

Effect of Inter-Modular Connection on Fast Sparse Synchronization in Clustered Small-World Neural Networks

Sang-Yoon Kim* and Woochang Lim†

*Institute for Computational Neuroscience and Department of Science Education,
Daegu National University of Education, Daegu 705-115, Korea*

Abstract

We consider a clustered network with small-world sub-networks of inhibitory fast spiking interneurons, and investigate the effect of inter-modular connection on emergence of fast sparsely synchronized rhythms by varying both the inter-modular coupling strength J_{inter} and the average number of inter-modular links per interneuron $M_{syn}^{(inter)}$. In contrast to the case of non-clustered networks, two kinds of sparsely synchronized states such as modular and global synchronization are found. For the case of modular sparse synchronization, the population behavior reveals the modular structure, because the intra-modular dynamics of sub-networks make some mismatching. On the other hand, in the case of global sparse synchronization, the population behavior is globally identical, independently of the cluster structure, because the intra-modular dynamics of sub-networks make perfect matching. We introduce a realistic cross-correlation modularity measure, representing the matching-degree between the instantaneous sub-population spike rates of the sub-networks, and examine whether the sparse synchronization is global or modular. Depending on its magnitude, the inter-modular coupling strength J_{inter} seems to play “dual” roles for the pacing between spikes in each sub-network. For large J_{inter} , due to strong inhibition it plays a destructive role to “spoil” the pacing between spikes, while for small J_{inter} it plays a constructive role to “favor” the pacing between spikes. Through competition between the constructive and the destructive roles of J_{inter} , there exists an intermediate optimal J_{inter} at which the pacing degree between spikes becomes maximal. In contrast, the average number of inter-modular links per interneuron $M_{syn}^{(inter)}$ seems to play a role just to favor the pacing between spikes. With increasing $M_{syn}^{(inter)}$, the pacing degree between spikes increases monotonically thanks to the increase in the degree of effectiveness of global communication between spikes. Furthermore, we employ the realistic sub- and whole-population order parameters, based on the instantaneous sub- and whole-population spike rates, to determine the threshold values for the synchronization-unsynchronization transition in the sub- and whole-populations, and the degrees of global and modular sparse synchronization are also measured in terms of the realistic sub- and whole-population statistical-mechanical spiking measures defined by considering both the occupation and the pacing degrees of spikes. It is expected that our results have important implications for the role of the brain plasticity.

PACS numbers: 87.19.lm, 87.19.lc

Keywords: Clustered small-world network, Effect of inter-modular connection, Fast sparsely synchronized rhythm

*Electronic address: sykim@icn.re.kr

†Electronic address: wclim@icn.re.kr

I. INTRODUCTION

Recently, much attention has been paid to brain rhythms in health and disease [1, 2]. Particularly, we are interested in fast sparsely synchronized cortical rhythms which are associated with diverse cognitive functions such as sensory perception, feature integration, selective attention, and memory formation [3]. At the population level, local field potential recordings have been observed to show synchronous fast oscillations [e.g., gamma rhythm (30-100 Hz) and ultrafast sharp-wave ripple (100-200 Hz)], while individual neuronal recordings have been found to exhibit stochastic and intermittent spike discharges [4–10]. Thus, single-cell firing activity differs markedly from the population oscillatory behavior. These sparsely synchronized rhythms are in contrast to fully synchronized rhythms. For the case of full synchronization, individual neurons fire regularly at the population frequency like the clock oscillators [11]. Hence, the fully synchronized oscillations may be well described by using the conventional coupled-oscillator model composed of suprathreshold spiking neurons above a threshold in the absence of noise or for weak noise [12]. However, such coupled-oscillator models are not adequate for describing sparse synchronization because individual neurons fire stochastically at low rates like the Geiger counters. Brunel et al. in [13–18] developed a framework appropriate for description of fast sparse synchronization by taking an opposite view from that of coupled oscillators. Under the condition of strong external noise, suprathreshold spiking neurons discharge irregular firings as Geiger counters, and then the population state becomes unsynchronized. However, when inhibitory recurrent feedback becomes sufficiently strong, this asynchronous state may be destabilized, and then a synchronous population state with irregular and intermittent individual discharges emerges. For this case, average total (external excitatory plus recurrent inhibitory) input current into individual neurons is subthreshold, but stochastic and intermittent firings are triggered when fluctuations (due to noise in external and recurrent inputs) cross a threshold. In this way, under the balance between strong external noise and strong recurrent inhibition, fast sparse synchronization was found to occur in networks of suprathreshold neurons [13–18]. Similar sparsely synchronized rhythms were also found to appear via cooperation of noise-induced spikings of subthreshold neurons (which can not fire spontaneously without noise) [19–21]. However, in contrast to the above works on suprathreshold neurons, sparse synchronization for the case of subthreshold neurons has been found to appear under relatively weak external

noise and recurrent inhibition, and the sparsely synchronized rhythms were also found to be slow when compared with the suprathreshold case.

In this paper, we are concerned about emergence of fast sparsely synchronized rhythms in an ensemble of suprathreshold neurons, as in the previous works of Brunel et al. [13–18] where both random and global synaptic couplings were considered. However, connection architecture of the real brain has been found to have complex topology which is neither regular nor random [22–30]. Particularly, the mammalian brain (e.g., cat and macaque) has been revealed to have a modular structure composed of sparsely linked clusters with spatial localization [31–34]. Within each cluster, neurons are more densely linked and exhibit similar connectional and functional features. This clustered organization of the brain network reveals the anatomical substrate for segregation which refers to the subdivision of the brain into regions specialized in particular functional tasks [35–37]. This segregation allows the brain to process information in parallel, simultaneously by distinct populations of neurons. However, for emergence of a coherent perception and comprehensive understanding of the environment as a whole, specialized information of different modalities and features should be integrated. This integration refers to the capacity of a system to collect information of different nature and combine it to produce new useful information. For example, sensory perception requires the binding of the features of a receptive field (e.g., color, orientation, and position of a visual object). In this way, brain connectivity should be organized into a balance between segregation (specialization) and integration (binding) [38–42]. Here, we extend the previous works [13–18] to realistic brain networks by taking into consideration the modular structure of the real brain. For modeling the modular structure of real brain, we consider a clustered network composed of sparsely connected sub-networks. The sub-networks stand for the modules (clusters) of the brain. As is also known, the connection structure in each module of the real brain reveals complex topology such as small-worldness and scale-freeness [22–30]. Here, each sub-network (representing a cluster) is modeled as the Watts-Strogatz small-world network which interpolates between the regular lattice with high clustering (i.e., high cliquishness of a typical neighborhood) and the random graph with short path length (i.e., average short separation between two neurons represented by average number of synapses between two neurons along the minimal path) by varying the rewiring probability $p_{rewiring}$ from local to long-range connections; $p_{rewiring} = 0$ and 1 correspond to the regular lattice and the random graph, respectively [43–45]. The Watts-Strogatz

model for the small-world sub-network may be regarded as a cluster-friendly extension of the random network by reconciling the six degrees of separation (small-worldness) [46, 47] with the circle of friends (clustering). Many recent works on various subjects of neurodynamics have been done in small-world networks with predominantly local connections and rare long-distance connections [48–59]. Effect of this small-world connectivity on fast sparse synchronization has also been studied in our recent work [60].

We note that real brain networks consisting of modules are far more complex than minimal (non-modular) models such as small-world and scale-free networks. The main purpose of this study is to extend previous works on sparse synchronization in non-modular regular, random, small-world, and scale-free networks [13–18, 60, 61] to the case of modular networks. Clustered neural networks composed of regular, small-world, and scale-free sub-networks have been employed for study on several subjects of neurodynamics [35–37, 62–65]. For our aim, we consider a clustered network with small-world sub-networks of inhibitory spiking neurons, and investigate the effect of inter-modular connection on emergence of fast sparsely synchronized rhythms. In the absence of inter-modular coupling, we consider three cases for the intra-modular dynamics in sub-networks: (1) synchronized in all identical sub-networks, (2) unsynchronized in all identical sub-networks, and (3) synchronized/unsynchronized in non-identical sub-networks. For each case, we study the population states by changing both the inter-modular coupling strength J_{inter} and the average number of inter-modular links per interneuron $M_{syn}^{(inter)}$. Consequently, two kinds of sparse synchronization such as modular and global synchronization are found, in contrast to the case of non-modular networks. For the case of modular sparse synchronization, the population behavior reveals the modular structure, and hence the degree of sparse synchronization in the whole population becomes less than that in the sub-networks, because the intra-modular dynamics of sub-networks make some mismatching. In contrast, for the case of global sparse synchronization, the population behavior is globally identical, independently of the cluster structure, because the intra-modular dynamics of sub-networks make perfect matching. For large J_{inter} it plays a destructive role to spoil the pacing between sparse spikes, because of strong inhibition. Hence, when passing a large threshold a transition to unsynchronization occurs. However, for small J_{inter} it plays a constructive role to favor the pacing between spikes in each sub-network. Hence, via competition between the constructive and the destructive roles of J_{inter} , there appears an intermediate optimal J_{inter} at which the pacing degree between

spikes becomes maximal. In this way, J_{inter} plays dual roles for the pacing between spikes in each sub-network, depending on its magnitude. On the other hand, the average number of inter-modular links per interneuron $M_{syn}^{(inter)}$ plays a role just to favor the pacing between spikes. As $M_{syn}^{(inter)}$ is increased, the pacing degree between spikes increases monotonically due to the increase in the degree of effectiveness of global communication between spikes. To make characterization of the synchronization-unsynchronization transitions in the sub- and whole-populations, we employ the realistic sub- and whole-population order parameters, based on the instantaneous sub- and whole-population spike rates [66]. Moreover, we introduce a realistic cross-correlation modularity measure, representing the matching-degree between the instantaneous sub-population spike rates of sub-networks, and examine whether the sparse synchronization is global or modular. The degrees of modular and global sparse synchronization are also measured in terms of the realistic sub- and whole-population statistical-mechanical spiking measures defined by considering both the occupation and the pacing degrees of the spikes [66].

This paper is organized as follows. In Sec. II, we describe a clustered network with small-world sub-networks of inhibitory fast spiking (FS) interneurons. In Sec. III, we investigate the effect of inter-modular connection on emergence of fast sparsely synchronized rhythms by varying both J_{inter} and $M_{syn}^{(inter)}$. Finally, a summary is given in Section IV.

II. CLUSTERED SMALL-WORLD NETWORK OF INHIBITORY FS IZHKE-VICH INTERNEURONS

A neural circuit in the major parts of the brain is composed of a few types of excitatory principal cells and diverse types of inhibitory interneurons. Interneuronal networks play the role of the backbones of many brain rhythms by providing a synchronous oscillatory output to the principal cells [1, 3, 12, 23]. Here, we consider a clustered network with M ($= 3$) small-world sub-networks. Each small-world sub-network consists of L inhibitory interneurons equidistantly placed on a one-dimensional ring of radius $L/2\pi$. For illustrative purpose, an example of the clustered network topology is shown in Fig. 1. Each of the three sub-networks, consisting of $L = 20$ interneurons, is modeled as the Watts-Strogatz small-world network which interpolates between the regular lattice and the random graph by varying the rewiring probability $p_{rewiring}$ from local to long-range connections [43–45].

We start from the case of $p_{rewiring} = 0$, corresponding to a directed regular ring lattice where each interneuron is coupled to its first $M_{syn}^{(intra)}$ ($= 4$) neighbors ($M_{syn}^{(intra)}/2$ on either side) via outward synapses. Then, we rewire each outward connection at random with probability $p_{rewiring}$ such that self-connections and duplicate connections are excluded, and the value of $p_{rewiring}$ is 0.25 for the case of Fig. 1. Within each small-world sub-network, the average number of intra-modular synaptic inputs per interneuron is $M_{syn}^{(intra)}$, while there exist 8 sparse random inter-modular links between small-world sub-networks. As an element in our neural system, we choose the FS Izhikevich interneuron model which is not only biologically plausible, but also computationally efficient [67–70]. The population dynamics in this neural network is governed by the following set of ordinary differential equations:

$$C \frac{dv_i^{(I)}}{dt} = k(v_i^{(I)} - v_r)(v_i^{(I)} - v_t) - u_i^{(I)} + I_{DC} + D\xi_i^{(I)} - I_{I,i}^{(intra,syn)} - I_{I,i}^{(inter,syn)}, \quad (1)$$

$$\frac{du_i^{(I)}}{dt} = a\{U(v_i^{(I)}) - u_i^{(I)}\}, \quad i = 1, \dots, L, \quad I = 1, \dots, M, \quad (2)$$

with the auxiliary after-spike resetting:

$$\text{if } v_i^{(I)} \geq v_p, \text{ then } v_i^{(I)} \leftarrow c \text{ and } u_i^{(I)} \leftarrow u_i^{(I)} + d, \quad (3)$$

where

$$U(v) = \begin{cases} 0 & \text{for } v < v_b \\ b(v - v_b)^3 & \text{for } v \geq v_b \end{cases}, \quad (4)$$

$$I_{I,i}^{(intra,syn)} = \frac{J_{intra}}{d_{I,i}^{intra}} \sum_{j=1(\neq i)}^L w_{ij}^{(I,I)} s_j^{(I)}(t)(v_i^{(I)} - V_{syn}), \quad (5)$$

$$I_{I,i}^{(inter,syn)} = \frac{J_{inter}}{d_{I,i}^{inter}} \sum_{J=1(\neq I)}^M \sum_{j=1}^L w_{ij}^{(I,J)} s_j^{(J)}(t)(v_i^{(I)} - V_{syn}), \quad (6)$$

$$s_j^{(I)}(t) = \sum_{f=1}^{F_j^{(I)}} E(t - t_f^{(I,J)} - \tau_l); \quad E(t) = \frac{1}{\tau_d - \tau_r} (e^{-t/\tau_d} - e^{-t/\tau_r}) \Theta(t). \quad (7)$$

Here, the state of the i th neuron in the I th sub-network at a time t is characterized by two state variables: the membrane potential $v_i^{(I)}$ and the recovery current $u_i^{(I)}$. In Eq. (1), C is the membrane capacitance, v_r is the resting membrane potential, and v_t is the instantaneous threshold potential. After the potential reaches its apex (i.e., spike cutoff value) v_p , the membrane potential and the recovery variable are reset according to Eq. (3). The units of

the capacitance C , the potential v , the current u and the time t are pF, mV, pA, and ms, respectively.

Unlike Hodgkin-Huxley-type conductance-based models, the Izhikevich model matches neuronal dynamics by tuning the parameters instead of matching neuronal electrophysiology. The parameters k and b are associated with the neuron's rheobase and input resistance, a is the recovery time constant, c is the after-spike reset value of v , and d is the total amount of outward minus inward currents during the spike and affecting the after-spike behavior (i.e., after-spike jump value of u). Tuning these parameters, the Izhikevich neuron model may produce 20 of the most prominent neuro-computational features of cortical neurons [67–70]. Here, we use the parameter values for the FS interneurons (which do not fire postinhibitory rebound spikes) in the layer 5 rat visual cortex [69]; $C = 20$, $v_r = -55$, $v_t = -40$, $v_p = 25$, $v_b = -55$, $k = 1$, $a = 0.2$, $b = 0.025$, $c = -45$, $d = 0$.

Each Izhikevich interneuron is stimulated by using the common DC current I_{DC} (measured in units of pA) and an independent Gaussian white noise $\xi_i^{(I)}$ [see the 3rd and the 4th terms in Eq. (1)] satisfying $\langle \xi_i^{(I)}(t) \rangle = 0$ and $\langle \xi_i^{(I)}(t) \xi_j^{(J)}(t') \rangle = \delta_{IJ} \delta_{ij} \delta(t - t')$, where $\langle \dots \rangle$ denotes the ensemble average. The noise ξ is a parametric one that randomly perturbs the strength of the applied current I_{DC} , and its intensity is controlled by using the parameter D (measured in units of $\text{pA} \cdot \text{ms}^{1/2}$). In the absence of noise (i.e., $D = 0$), the Izhikevich interneuron exhibits a jump from a resting state to a spiking state via subcritical Hopf bifurcation for $I_{DC,h} = 73.7$ by absorbing an unstable limit cycle born via a fold limit cycle bifurcation for $I_{DC,l} = 72.8$. Hence, the Izhikevich interneuron shows type-II excitability because it begins to fire with a non-zero frequency [71, 72]. As I_{DC} is increased from $I_{DC,h}$, the mean firing rate f increases monotonically. Throughout this paper, we consider a suprathreshold case of $I_{DC} = 1500$, where the membrane potential v oscillates very fast with $f \simeq 633$ Hz; for more details, refer to Fig. 1 in [60].

The last two terms in Eq. (1) represent the intra- and the inter-modular synaptic couplings of the network. $I_{I,i}^{(intra,syn)}$ and $I_{I,i}^{(inter,syn)}$ of Eqs. (5) and (6) represent the intra- and the inter-modular synaptic currents injected into the i th neuron in the I th sub-network, respectively. The synaptic connectivity is given by the connection weight matrix $W (= \{w_{ij}^{(I,J)}\})$ where $w_{ij}^{(I,J)} = 1$ if the neuron j in the J th sub-network is presynaptic to the neuron i in the I th sub-network; otherwise, $w_{ij}^{(I,J)} = 0$. Here, the intra-modular synaptic connection is modeled in terms of the Watts-Strogatz small-world network. Then, the in-degree of the

i th neuron in the I th sub-network for the intra-modular synaptic connection, $d_{I,i}^{intra}$ (i.e., the number of intra-modular synaptic inputs to the neuron i in the I th sub-network) is given by $d_{I,i}^{intra} = \sum_{j=1(\neq i)}^L w_{ij}^{(I,I)}$. For this intra-modular case, the average number of intra-modular synaptic inputs per neuron is $M_{syn}^{(intra)} = \frac{1}{M \cdot L} \sum_{I=1}^M \sum_{i=1}^L d_{I,i}^{intra}$. In contrast to the intra-modular connection, the inter-modular synaptic connection is given randomly. Then, the in-degree of the i th neuron in the I th sub-network for the inter-modular synaptic connection, $d_{I,i}^{inter}$ (i.e., the number of inter-modular synaptic inputs to the neuron i in the I th sub-network) is given by $d_{I,i}^{inter} = \sum_{J=1(\neq I)}^M \sum_{j=1}^L w_{ij}^{(I,J)}$. In the inter-modular case, the average number of inter-modular synaptic inputs per neuron is $M_{syn}^{(inter)} = \frac{1}{M \cdot L} \sum_{I=1}^M \sum_{i=1}^L d_{I,i}^{inter}$, and these inter-modular links are randomly connected with the inter-modular connection probability $p_{inter} = \frac{M_{syn}^{(inter)}}{(M-1) \cdot L}$. Compared to the intra-modular connections, the inter-modular connections are sparse (i.e., $M_{syn}^{(inter)} < M_{syn}^{(intra)}$). The fraction of open synaptic ion channels at time t is denoted by $s(t)$. The time course of $s_j^{(I)}(t)$ of the j th neuron in the I th sub-network is given by a sum of delayed double-exponential functions $E(t - t_f^{(I,j)} - \tau_l)$ [see Eq. (7)], where τ_l is the synaptic delay, and $t_f^{(I,j)}$ and $F_j^{(I)}$ are the f th spiking time and the total number of spikes of the j th neuron in the I th sub-network at time t , respectively. Here, $E(t)$ [which corresponds to contribution of a presynaptic spike occurring at time 0 to $s(t)$ in the absence of synaptic delay] is controlled by the two synaptic time constants: synaptic rise time τ_r and decay time τ_d , and $\Theta(t)$ is the Heaviside step function: $\Theta(t) = 1$ for $t \geq 0$ and 0 for $t < 0$. For the inhibitory GABAergic synapse (involving the GABA_A receptors), $\tau_l = 1$ ms, $\tau_r = 0.5$ ms, and $\tau_d = 5$ ms [15]. The intra- and the inter-modular synaptic coupling strengths are controlled by the parameters J_{intra} and J_{inter} (measured in units of μS), respectively and V_{syn} is the synaptic reversal potential. Here, we use $V_{syn} = -80$ mV for the inhibitory synapse.

Numerical integration of Eqs. (1)-(2) is done using the Heun method [73] (with the time step $\Delta t = 0.01$ ms). For each realization of the stochastic process, we choose a random initial point $[v_i^{(I)}(0), u_i^{(I)}(0)]$ for the i th ($i = 1, \dots, N$) neuron in the I th sub-network with uniform probability in the range of $v_i^{(I)}(0) \in (-50, -45)$ and $u_i^{(I)}(0) \in (10, 15)$.

III. EFFECT OF INTER-MODULAR CONNECTION ON FAST SPARSELY SYNCHRONIZED RHYTHMS

In order to extend previous works on fast sparse synchronization in non-modular networks [13–18, 60, 61] to the case of modular networks, we consider a clustered small-world network of inhibitory FS Izhikevich interneurons, and investigate the effect of inter-modular connection on emergence of fast sparsely synchronized rhythms by varying both the inter-modular coupling strength J_{inter} and the average number of inter-modular links per interneuron $M_{syn}^{(inter)}$. In contrast to the case of non-modular networks, two kinds of sparsely synchronized states such as modular and global sparse synchronization are thus found, and characterizations of these sparsely synchronized states are also made by employing diverse realistic measures, based on instantaneous sub- and whole-population spike rates.

In the absence of inter-modular coupling, we consider three cases for the intra-modular dynamics in the Watts-Strogatz small-world sub-networks: (1) synchronized in all identical sub-networks, (2) unsynchronized in all identical sub-networks, and (3) synchronized/unsynchronized in non-identical sub-networks. For each case, we study emergence of sparsely synchronized population states by changing both J_{inter} and $M_{syn}^{(inter)}$. Throughout this paper, we fix the DC current strength I_{DC} and the noise intensity D (applied to individual neurons) at $I_{DC} = 1500$ and $D = 500$, respectively, and the average number of intra-modular synaptic inputs per interneuron $M_{syn}^{(intra)}$ and the intra-modular coupling strength $J_{syn}^{(intra)}$ are also fixed at $M_{syn}^{(intra)} = 50$ and $J_{syn}^{(intra)} = 1400$. We start from the 1st case of intra-modular dynamics where the rewiring probability in every sub-network is $p_{rewiring} = 0.25$. In computational neuroscience, an ensemble-averaged sub-population potential $V_s^{(I)}(t)$ for the I th sub-network ($I = 1, 2, 3$), containing L FS Izhikevich interneurons,

$$V_s^{(I)}(t) = \frac{1}{L} \sum_{i=1}^L v_i^{(I)}(t), \quad (8)$$

and an ensemble-averaged whole-population potential for the whole network with M ($=3$) sub-networks,

$$V_w(t) = \frac{1}{M} \sum_{I=1}^M V_s^{(I)}(t), \quad (9)$$

are often used for describing emergence of population neural synchronization in the sub- and the whole-populations, respectively (e.g., sparse synchronization in a population of

subthreshold neurons was described in terms of an ensemble-averaged global potential [19–21]). However, to directly obtain $V_s^{(I)}(t)$ and $V_w(t)$ in real experiments is very difficult. To overcome this difficulty, instead of $V_s^{(I)}(t)$ and $V_w(t)$, we use an experimentally-obtainable instantaneous sub- and whole-population spike rates which are often used as collective quantities showing sub- and whole-population behaviors [3, 13–18, 60, 61, 66]. The instantaneous sub-population spike rate (ISPSR) $R_s^{(I)}(t)$ is obtained from the raster plot of neural spikes which is a collection of spike trains of individual neurons in the I th sub-population. Such raster plots of spikes, where sub-population spike synchronization may be well visualized, are fundamental data in experimental neuroscience. For the synchronous case, “stripes” (composed of spikes and indicating sub-population synchronization) are found to be formed in the raster plot. Hence, for a synchronous case, an oscillating ISPSR appears, while for an unsynchronized case the ISPSR is nearly stationary. To obtain a smooth ISPSR, we employ the kernel density estimation (kernel smoother) [74]. Each spike in the raster plot is convoluted (or blurred) with a kernel function $K_h(t)$ to obtain a smooth estimate of ISPSR for the I th sub-network, $R_s^{(I)}(t)$:

$$R_s^{(I)}(t) = \frac{1}{L} \sum_{i=1}^L \sum_{s=1}^{n_i^{(I)}} K_h(t - t_s^{(I,i)}), \quad (10)$$

where $t_s^{(I,i)}$ is the s th spiking time of the i th neuron in the I th sub-network, $n_i^{(I)}$ is the total number of spikes for the i th neuron in the I th sub-network, and we use a Gaussian kernel function of band width h :

$$K_h(t) = \frac{1}{\sqrt{2\pi}h} e^{-t^2/2h^2}, \quad -\infty < t < \infty. \quad (11)$$

Then, the instantaneous whole-population spike rate (IWPSR) kernel estimate $R_w(t)$ for the whole population is given by an average of the ISPSR kernel estimates of the $M(= 3)$ sub-populations:

$$R_w(t) = \frac{1}{M} \sum_{I=1}^M R_s^{(I)}(t). \quad (12)$$

In the absence of inter-modular coupling (i.e., $J_{inter} = 0$), every sub-population in the small-world sub-networks exhibits identical sparse synchronization, as shown in Fig. 2. Clear stripes are formed in the raster plot of Fig. 2(a). The density of stripes is sparse because only a small fraction (about 0.22) of the total $L (= 10^3)$ neurons in the sub-population fire in each stripe. Due to presence of these sparse stripes, the ISPSR kernel estimate $R_s^{(I)}(t)$

shows fast regular oscillation with sub-population frequency $f_p^{(I)} \simeq 147$ Hz, as shown in Figs. 2(b)-2(c). For the case of individual neurons, the inter-spike interval (ISI) histogram has multiple peaks appearing at multiples of the period T_I ($\simeq 6.8$ ms) of $R_s^{(I)}(t)$ (i.e., skipping of spikes occurs at random integer multiples of T_I) [see Fig. 2(d)]. Because of this stochastic spike skipping (also called the stochastic phase locking) [19–21, 60, 61, 66, 75–77], individual neurons exhibit stochastic and intermittent spike discharges, and hence partial occupation occurs in the stripes of the raster plot. In contrast to sub-population rhythms, the distribution of mean firing rates (MFRs) of individual neurons shows a peak near $f_i^{(I)}$ ($\simeq 33$ Hz) which is much less than the sub-population frequency $f_p^{(I)}$ [see Fig. 2(e)]. In this way, firing activity of individual neurons differs distinctly from the population oscillatory behavior for the case of sparse synchronization [3, 13–18, 60, 61, 66]. For more details on the sparse synchronization in the (non-modular) small-world network, refer to [60].

From now on, we investigate the effect of inter-modular connection on sparse synchronization for the 1st case of intra-modular dynamics by changing the inter-modular coupling strength J_{inter} for $M_{syn}^{(inter)} = 20$. Figures 3(a)-3(c) show the raster plots of spikes in the three sub-populations for $J_{inter} = 10, 500$, and 2500 , respectively. The corresponding ISPSR and IWPSR kernel estimates, $R_s^{(I)}(t)$ and $R_w(t)$, for $J_{inter} = 10, 500$, and 2500 are also shown in Figs. 3(d1)-3(f4), respectively. For small J_{inter} , the inter-modular coupling strength plays a constructive role to favor the pacing between spikes in each sub-network, as shown in the case of $J_{inter} = 10$. For each I th sub-population, sparse stripes are formed in the raster plot and $R_s^{(I)}(t)$ shows a regular oscillation, as shown in Fig. 3(a) and Figs. 3(d1)-3(d4). Hence, each sub-population exhibits sparse synchronization. However, the intra-modular dynamics of sub-networks make some mismatching because both the stripes and the ISPSRs between the sub-networks are shifted. Vertical gray lines which pass minima of $R_w(t)$ are drawn as reference lines for matching between $R_s^{(I)}(t)$ ($I = 1, 2, 3$) [where the minima of $R_s^{(I)}(t)$ [$R_w(t)$] are denoted by solid (open) circles]. As a result of mismatching, the degree of sparse synchronization in the whole population becomes less than that in the sub-networks [i.e., the amplitude of $R_w(t)$ is less than that of $R_s^{(I)}(t)$], and this kind of population behavior for $J_{inter} = 10$ is referred to as the modular sparse synchronization because it reveals the modular structure. With increasing J_{inter} , the mismatching degree between the intra-modular dynamics of sub-networks decreases, although the stripes in the raster plots become more sparse due to increased inhibition. Eventually when passing a threshold

J_{inter}^* ($\simeq 268$), intra-modular dynamics of sub-networks begin to make perfect matching. As a result, the population behavior becomes globally identical, independently of the cluster structure, as shown in Fig. 3(b) and Figs. 3(e1)-3(e4) for $J_{inter} = 500$ [where all the minima of $R_s^{(I)}(t)$ ($I = 1, 2, 3$) lie on the reference vertical line passing the minima of $R_w(t)$], and it is referred to as the global sparse synchronization. However, for sufficiently large J_{inter} , due to strong inhibition the inter-modular coupling strength plays a destructive role to spoil the pacing between sparse spikes. Hence, as J_{inter} passes a higher critical value $J_{inter,h}^*$ ($\simeq 1657$) the global sparse synchronization breaks into unsynchronization. As an example, refer to the case of $J_{inter} = 2500$. Sparse spikes in the raster plot of each sub-network are completely scattered without forming any stripes [see Fig. 3(c)], and hence each ISPSR kernel estimate $R_s^{(I)}(t)$ becomes nearly stationary (i.e., every sub-network exhibits an unsynchronized state), as shown in Figs. 3(f1)-3(f4). We now vary not only J_{inter} but also $M_{syn}^{(inter)}$, and investigate emergence of population spike synchronization in the J_{inter} - $M_{syn}^{(inter)}$ plane. Thus, we obtain the state diagram in Fig. 3(g). Modular sparse synchronization emerges for small J_{inter} or $M_{syn}^{(inter)}$ in the “L”-shaped gray region, while in the dark gray region global sparse synchronization appears. For large J_{inter} (> 1572), unsynchronization occurs between the modular and the global synchronization. Changes in the population behaviors along the routes I, II, and III in Fig. 3(g) are given below.

We first consider the case of route I for $M_{syn}^{(inter)} = 20$. Some results for this case are given for $J_{inter} = 10, 500$, and 2500 in Figs. 3(a)-3(f4). As J_{inter} is increased, a transition from modular sparse synchronization to global sparse synchronization [when passing a threshold J_{inter}^* ($\simeq 268$)], and eventually to unsynchronization [when passing a higher threshold $J_{inter,h}^*$ ($\simeq 1657$)] occurs. As is well known, a conventional order parameter, based on the ensemble-averaged global potential, is often used for describing transition from synchronization to unsynchronization in computational neuroscience [19–21, 78–80]. Recently, instead of the global potential, we used an experimentally-obtainable instantaneous population spike rate kernel estimate, and developed a realistic order parameter for the case of the non-modular networks, which may be applicable in both the computational and the experimental neuroscience [66]. For the case of modular networks, the mean square deviation of the ISPSR kernel estimate $R_s^{(I)}(t)$ for the I th sub-network ($I=1, 2, 3$),

$$\mathcal{O}_s^{(I)} \equiv \overline{(R_s^{(I)}(t) - \overline{R_s^{(I)}(t)})^2}, \quad (13)$$

and the mean square deviation of the IWPSR kernel estimate $R_w(t)$ for the whole network,

$$\mathcal{O}_w \equiv \overline{(R_w(t) - \overline{R_w(t)})^2}, \quad (14)$$

play the role of realistic sub- and whole-population order parameters $\mathcal{O}_s^{(I)}$ and \mathcal{O}_w to determine a threshold for the synchronization-unsynchronization transition, where the overbar represents the time average. The order parameters $\mathcal{O}_s^{(I)}$ and \mathcal{O}_w , representing the time-averaged fluctuations of $R_s^{(I)}(t)$ and $R_w(t)$, approach non-zero (zero) limit values for the synchronized (unsynchronized) state in the thermodynamic limit of $L \rightarrow \infty$. These order parameters may be regarded as thermodynamic measures because they concern just the macroscopic ISPSR and IWPSR kernel estimates $R_s^{(I)}(t)$ and $R_w(t)$ without any consideration between the macroscopic ISPSR and IWPSR kernel estimates and microscopic individual spikes. Figures 4(a1)-4(a4) show plots of the sub- and the whole-population order parameters $\langle \mathcal{O}_s^{(I)} \rangle_r$ and $\langle \mathcal{O}_w \rangle_r$ versus J_{inter} , where $\langle \cdots \rangle_r$ denotes an average over realizations. For $J_{inter} < J_{inter,h}^*$ ($\simeq 1657$), synchronized states exist because the values of $\langle \mathcal{O}_s^{(I)} \rangle_r$ and $\langle \mathcal{O}_w \rangle_r$ become saturated to non-zero limit values for large L . When passing the higher threshold $J_{inter,h}^*$, a transition to unsynchronization occurs because the order parameters $\langle \mathcal{O}_s^{(I)} \rangle_r$ and $\langle \mathcal{O}_w \rangle_r$ tend to zero as $L \rightarrow \infty$. These unsynchronized states seem to appear due to a destructive effect of strong inhibition spoiling the pacing between sparse spikes. Here, we present two explicit examples for the synchronized and the unsynchronized states. First, we consider the synchronized case for $J_{inter} = 1600$. For $L = 10^3$, sparse stripes are formed in the raster plot of spikes for each sub-network, and the ISPSR and the IWPSR kernel estimates $R_s^{(I)}(t)$ and $R_w(t)$ show regular oscillations, although there are some variations in the amplitudes [see Figs. 4(b) and 4(d)]. As L is increased to $L = 10^4$, stripes in the raster plots become more clear, and $R_s^{(I)}(t)$ and $R_w(t)$ display more regular oscillations with nearly the same amplitudes, as shown in Figs. 4(c) and 4(e). Consequently, the population state for $J_{inter} = 1600$ seems to be synchronized because $R_s^{(I)}(t)$ and $R_w(t)$ tend to show more regular oscillations as L goes to the infinity. As a second example, we consider the unsynchronized case of $J_{inter} = 1700$. As shown in Fig. 4(f) for $L = 10^3$, sparse spikes are scattered without forming any stripes in the raster plot, and $R_s^{(I)}(t)$ and $R_w(t)$ in Fig. 4(h) show little noisy fluctuations. In contrast to the synchronized case, as L is increased to $L = 10^4$, sparse spikes become more scattered, and consequently $R_s^{(I)}(t)$ and $R_w(t)$ become nearly stationary, as shown in Figs. 4(g) and 4(i). Hence, the population state

for $J_{inter} = 1700$ seems to be unsynchronized because $R_s^{(I)}(t)$ and $R_w(t)$ tend to be nearly stationary as L increases to the infinity.

In order to further understand the above synchronization-unsynchronization transition, we investigate the effect of inter-modular connection on the “microscopic” dynamical cross-correlations between neuronal pairs. As examples, we reconsider the same cases of $J_{inter} = 1600$ and 1700 as in Fig. 4. For obtaining dynamical pair cross-correlations, each spike train of the i th neuron in the I th sub-network is convoluted with a Gaussian kernel function $K_h(t)$ of band width h to get a smooth estimate of instantaneous individual spike rate (IISR) $r_i^{(I)}(t)$:

$$r_i^{(I)}(t) = \sum_{s=1}^{n_i^{(I)}} K_h(t - t_s^{(I,i)}), \quad (15)$$

where $t_s^{(I,i)}$ is the s th spiking time of the i th neuron in the I th sub-network, $n_i^{(I)}$ is the total number of spikes for the i th neuron, and $K_h(t)$ is given in Eq. (11). Then, the normalized temporal cross-correlation function $C_{i,j}^{(I)}(\tau)$ between the IISR kernel estimates $r_i^{(I)}(t)$ and $r_j^{(I)}(t)$ of the (i, j) neuronal pair in the I th sub-network is given by:

$$C_{i,j}^{(I)}(\tau) = \frac{\overline{\Delta r_i^{(I)}(t + \tau) \Delta r_j^{(I)}(t)}}{\sqrt{\overline{\Delta r_i^{(I)}(t)^2}} \sqrt{\overline{\Delta r_j^{(I)}(t)^2}}}, \quad (16)$$

where $\Delta r_i^{(I)}(t) = r_i^{(I)}(t) - \overline{r_i^{(I)}(t)}$ and the overline denotes the time average. Similar to the case of non-modular small-world network [60], we now introduce the spatial cross-correlation function $C_l^{(I)}$ ($l = 1, \dots, L/2$) between neuronal pairs separated by a spatial distance l in the I th sub-network through average of all the temporal cross-correlations between $r_i^{(I)}(t)$ and $r_{i+l}^{(I)}(t)$ ($i = 1, \dots, L$) at the zero-time lag:

$$C_l^{(I)} = \frac{1}{L} \sum_{i=1}^L C_{i,i+l}^{(I)}(0) \quad \text{for } l = 1, \dots, L/2. \quad (17)$$

Here, if $i + l > L$ in Eq. (17), then $i + l - L$ is considered instead of $i + l$ because neurons lie on the ring. Figure 5(a1) shows the plots of the spatial cross-correlation functions $C_l^{(I)}$ versus l for $L = 10^3$ in the case of $J_{inter} = 1600$. These spatial correlation functions $C_l^{(I)}$ are nearly non-zero constant ($\simeq 0.04$) in the whole range of l , and hence the correlation length η_I becomes $L/2$ ($=500$) covering the whole sub-networks (note that the maximal distance between neurons is $L/2$ because of the ring architecture on which neurons exist).

Consequently, each sub-network is composed of just one single synchronized block. For $L = 10^4$, the flatness of $C_l^{(I)}$ in Fig. 5(a2) also extends to the whole range ($l = L/2 = 5000$) of the I th sub-network, and hence the correlation length becomes $\eta_I = 5000$, which also covers the whole sub-network. In this way, for $J_{inter} = 1600$, due to a constructive role of J_{inter} favoring the pacing between sparse spikes, the correlation length η_I seems to cover the whole sub-network, independently of L . For this case, the normalized correlation length $\tilde{\eta}_I (= \frac{\eta_I}{L})$, representing the ratio of the correlation length η_I to the sub-network size L (i.e., denoting the relative size of synchronized blocks when compared to the whole sub-network size), has a non-zero limit value, $1/2$, and consequently synchronization emerges in each sub-network. In contrast, for $J_{inter} = 1700$ the spatial cross-correlation functions $C_l^{(I)}$ are nearly zero, independently of L , as shown in Figs. 5(b1)-5(b2). For this case, due to a destructive role of J_{inter} spoiling the pacing between sparse spikes, the correlation length η_I becomes nearly zero, and hence no synchronization occurs in each sub-network.

We now investigate the type of synchronization through measurement of the matching degree between the intra-modular dynamics of sub-networks in the synchronized range of $0 < J_{inter} < J_{inter,h}^* (\simeq 1657)$ along the route I in Fig. 3(g). Figures 6(a1)-6(a5) show the raster plots of spikes in the three sub-networks for $J_{inter} = 10, 30, 70, 400$, and 1200 , respectively. The ISPSR and the IWPSR kernel estimates, $R_s^{(I)}(t)$ and $R_w(t)$, for $J_{inter} = 10, 30, 70, 400$, and 1200 are also shown in Figs. 6(b1)-6(b5), respectively. For each I th sub-population, sparse stripes are formed in the raster plot of spikes and the ISPSR kernel estimate $R_s^{(I)}(t)$ shows a regular oscillation with global frequency $f_p^{(I)} \simeq 147$ Hz. Hence, each sub-population shows sparse synchronization. For the case of modular sparse synchronization for $J_{inter} = 10, 30$, and 70 , the intra-modular dynamics of sub-networks make some mismatching because both the stripes and the ISPSR kernel estimates between the sub-networks are shifted [see Figs. 6(b1)-6(b3) where the minima of $R_s^{(I)}(t)$ (denoted by solid circles) lie off the reference vertical lines which pass the minima of $R_w(t)$ (represented by open circles)]. Hence the amplitude of $R_w(t)$ becomes less than that of $R_s^{(I)}(t)$. As J_{inter} is increased, the mismatching degree decreases, and hence the amplitude of $R_w(t)$ increases. Eventually, when passing a threshold $J_{inter}^* (\simeq 268)$ global sparse synchronization occurs. Hence, for $J_{inter} = 400$ and 1200 , intra-modular dynamics of sub-networks (shown in their raster plots and ISPSR kernel estimates) make perfect matching [i.e., the minima of $R_s^{(I)}(t)$ lie on the reference vertical lines, as shown in Figs. 6(b4)-6(b5)], and hence the amplitude of $R_w(t)$ becomes the same as

that of $R_s^{(I)}(t)$. To determine the type of synchronization (modular or global), we measure the matching degree between the intra-modular dynamics of sub-networks in terms of the cross-correlation modularity measure C_M , based on ISPSRs. The normalized temporal cross-correlation function $C_{I,J}(\tau)$ between the ISPSR kernel estimates $R_s^{(I)}(t)$ and $R_s^{(J)}(t)$ of the I th and the J th sub-networks is given by:

$$C_{I,J}(\tau) = \frac{\overline{\Delta R_s^{(I)}(t+\tau)\Delta R_s^{(J)}(t)}}{\sqrt{\overline{\Delta R_s^{(I)}(t)^2}}\sqrt{\overline{\Delta R_s^{(J)}(t)^2}}}, \quad (18)$$

where $\Delta R_s^{(I)}(t) = R_s^{(I)}(t) - \overline{R_s^{(I)}(t)}$ and the overline denotes the time average. Figures 6(c1)-6(c5) show the normalized temporal cross-correlation functions $C_{I,J}(\tau)$ for $J_{inter} = 10, 30, 70, 400$, and 1200, respectively. Then, the cross-correlation modularity measure C_M is obtained through average of the temporal cross-correlations between all the sub-population pairs at the zero-time lag:

$$C_M = \frac{2}{M(M-1)} \sum_{I=1}^M \sum_{J=I+1}^M C_{I,J}(0). \quad (19)$$

When compared with the correlation modularity measure [35], based on sub-population potentials $V_s^{(I)}(t)$, C_M of Eq. (19), based on the experimentally-obtainable $R_s^{(I)}(t)$, is a more realistic one. Figure 6(d) shows the plot of $\langle C_M \rangle_r$ versus J_{inter} where $\langle \cdots \rangle_r$ denotes average over realizations. As J_{inter} is increased, $\langle C_M \rangle_r$ increases monotonically, and eventually when passing a threshold J_{inter}^* ($\simeq 268$), its value becomes 1. Hence, for $J_{inter} < J_{inter}^*$ modular sparse synchronization (with $\langle C_M \rangle_r < 1$) emerges, while global sparse synchronization (with $\langle C_M \rangle_r = 1$) appears for $J_{inter}^* < J_{inter} < J_{inter,h}^*$.

We also measure the degree of modular and global sparse synchronization in terms of realistic statistical-mechanical sub- and whole-population spiking measures, based on the ISPSR and the IWPSR kernel estimates $R_s^{(I)}(t)$ and $R_w(t)$ [66]. These realistic statistical-mechanical spiking measures are in contrast to the conventional statistical-mechanical spiking measures, based on the ensemble-averaged global potentials such as $V_s^{(I)}(t)$ and $V_w(t)$ of Eqs. (8) and (9) [19–21]. As shown in Figs. 6(a1)-6(a5), spike synchronization may be well visualized in the raster plots of spikes. For a synchronized case, the raster plot is composed of partially-occupied stripes (indicating sparse synchronization), and the corresponding ISPSR and IWPSR kernel estimates, $R_s^{(I)}(t)$ ($I = 1, 2, 3$) and $R_w(t)$, exhibit regular oscillations. Each i th ($i = 1, 2, 3, \dots$) global cycles of $R_s^{(I)}(t)$ and $R_w(t)$ begin from their left

minimum, pass the central maximum, and end at the right minimum [also, corresponding to the beginning point of the next $(i + 1)$ th global cycles]; the 1st global cycles of $R_s^{(I)}(t)$ and $R_w(t)$ appear after transient times of 10^3 ms, respectively. Spikes which appear in the i th global cycles of $R_s^{(I)}(t)$ and $R_w(t)$ form the i th stripes in the raster plots for the sub- and the whole-populations, respectively. To measure the degree of the sub- and the whole-population spike synchronization seen in the raster plots, statistical-mechanical sub- and whole-population measures $M_s^{(I)}$ and $M_s^{(w)}$, based on $R_s^{(I)}(t)$ and $R_w(t)$, are introduced by considering the occupation pattern and the pacing pattern of spikes in the stripes for the sub- and the whole-populations, which corresponds to a simple extension of the case of non-modular networks [66]. The sub- and the whole-population spiking measures $M_i^{(I)}$ ($I = 1, 2, 3$) and $M_i^{(w)}$ of the i th stripes [appearing in the i th global cycles of $R_s^{(I)}(t)$ and $R_w(t)$] are defined by the products of the sub- and the whole-population occupation degrees $O_i^{(I)}$ and $O_i^{(w)}$ of spikes (representing the density of the i th stripes) and the sub- and the whole-population pacing degrees $P_i^{(I)}$ and $P_i^{(w)}$ of spikes (denoting the smearing of the i th stripes), respectively:

$$M_i^{(I)} = O_i^{(I)} \cdot P_i^{(I)} \quad \text{and} \quad M_i^{(w)} = O_i^{(w)} \cdot P_i^{(w)}. \quad (20)$$

The sub- and the whole-population occupation degrees $O_i^{(I)}$ and $O_i^{(w)}$ in the i th stripes are given by the fractions of spiking neurons in the i th stripes:

$$O_i^{(I)} = \frac{N_{I,i}^{(s)}}{L} \quad \text{and} \quad O_i^{(w)} = \frac{N_{w,i}^{(s)}}{M \cdot L} \quad (21)$$

where $N_{I,i}^{(s)}$ and $N_{w,i}^{(s)}$ are the numbers of spiking neurons in the i th stripes for the I th sub-network and the whole network, respectively. For sparse synchronization with partially-occupied stripes, $O_i^{(I)} \ll 1$ and $O_i^{(w)} \ll 1$. The pacing degrees $P_i^{(I)}$ and $P_i^{(w)}$ of sparse spikes in the i th stripes for the sub- and the whole-populations can be determined in a statistical-mechanical way by taking into account their contributions to the macroscopic ISPSR and IWPSR kernel estimates $R_s^{(I)}(t)$ and $R_w(t)$, respectively. Instantaneous global phases $\Phi_s^{(I)}(t)$ of $R_s^{(I)}(t)$ and $\Phi_w(t)$ of $R_w(t)$ are introduced via linear interpolation in the two successive subregions forming global cycles [66, 81]. The global phases $\Phi_s^{(I)}(t)$ and $\Phi_w(t)$ between the left minimum (corresponding to the beginning point of the i th global cycle) and the central

maximum are given by

$$\Phi_s^{(I)}(t) = 2\pi(i - 3/2) + \pi \left(\frac{t - t_{I,i}^{(min)}}{t_{I,i}^{(max)} - t_{I,i}^{(min)}} \right) \quad \text{for } t_{I,i}^{(min)} \leq t < t_{I,i}^{(max)}, \quad (22)$$

$$\Phi_w(t) = 2\pi(i - 3/2) + \pi \left(\frac{t - t_{w,i}^{(min)}}{t_{w,i}^{(max)} - t_{w,i}^{(min)}} \right) \quad \text{for } t_{w,i}^{(min)} \leq t < t_{w,i}^{(max)}, \quad (23)$$

and $\Phi_s^{(I)}(t)$ and $\Phi_w(t)$ between the central maximum and the right minimum [corresponding to the beginning point of the $(i + 1)$ th global cycle] are given by

$$\Phi_s^{(I)}(t) = 2\pi(i - 1) + \pi \left(\frac{t - t_{I,i}^{(max)}}{t_{I,i+1}^{(min)} - t_{I,i}^{(max)}} \right) \quad \text{for } t_{I,i}^{(max)} \leq t < t_{I,i+1}^{(min)}, \quad (24)$$

$$\Phi_w(t) = 2\pi(i - 1) + \pi \left(\frac{t - t_{w,i}^{(max)}}{t_{w,i+1}^{(min)} - t_{w,i}^{(max)}} \right) \quad \text{for } t_{w,i}^{(max)} \leq t < t_{w,i+1}^{(min)}, \quad (25)$$

where $t_{I,i}^{(min)}$ and $t_{w,i}^{(min)}$ are the beginning times of the i th ($i = 1, 2, 3, \dots$) global cycles of $R_s^{(I)}(t)$ and $R_w(t)$ [i.e., the times at which the left minima of $R_s^{(I)}(t)$ and $R_w(t)$ appear in the i th global cycles], respectively, and $t_{I,i}^{(max)}$ and $t_{w,i}^{(max)}$ are the times at which the maxima of $R_s^{(I)}(t)$ and $R_w(t)$ appear in the i th global cycles, respectively. Then, the contributions of the k th microscopic spikes in the i th stripes occurring at the times $t_{I,k}^{(s)}$ and $t_{w,k}^{(s)}$ to $R_s^{(I)}(t)$ and $R_w(t)$ are given by $\cos \Phi_k^{(I)}$ and $\cos \Phi_k^{(w)}$, where $\Phi_k^{(I)}$ and $\Phi_k^{(w)}$ are the global phases at the k th spiking times [i.e., $\Phi_k^{(I)} \equiv \Phi_s^{(I)}(t_{I,k}^{(s)})$ and $\Phi_k^{(w)} \equiv \Phi_w(t_{w,k}^{(s)})$]. Microscopic spikes make the most constructive (in-phase) contributions to $R_s^{(I)}(t)$ and $R_w(t)$ when the corresponding global phases $\Phi_k^{(I)}$ and $\Phi_k^{(w)}$ are $2\pi n$ ($n = 0, 1, 2, \dots$), while they make the most destructive (anti-phase) contribution to $R_s^{(I)}(t)$ and $R_w(t)$ when $\Phi_k^{(I)}$ and $\Phi_k^{(w)}$ are $2\pi(n - 1/2)$. By averaging the contributions of all microscopic spikes in the i th stripes to $R_s^{(I)}(t)$ and $R_w(t)$, we obtain the pacing degrees $P_i^{(I)}$ and $P_i^{(w)}$ of spikes in the i th stripes:

$$P_i^{(I)} = \frac{1}{S_i^{(I)}} \sum_{k=1}^{S_i^{(I)}} \cos \Phi_k^{(I)} \quad \text{and} \quad P_i^{(w)} = \frac{1}{S_i^{(w)}} \sum_{k=1}^{S_i^{(w)}} \cos \Phi_k^{(w)}, \quad (26)$$

where $S_i^{(I)}$ and $S_i^{(w)}$ are the total numbers of microscopic spikes in the i th stripes for the sub- and the whole-population, respectively. By averaging $M_i^{(I)}$ and $M_i^{(w)}$ of Eq. (20) over a sufficiently large number N_s of stripes, we obtain the sub- and whole-population statistical-mechanical spiking measures $M_s^{(I)}$ and $M_s^{(w)}$:

$$M_s^{(I)} = \frac{1}{N_s} \sum_{i=1}^{N_s} M_i^{(I)} \quad \text{and} \quad M_s^{(w)} = \frac{1}{N_s} \sum_{i=1}^{N_s} M_i^{(w)}. \quad (27)$$

By varying J_{inter} , we follow 3×10^3 stripes (i.e., 3×10^3 global cycles) in each realization, and through an average over 20 realizations, we obtain the sub- and the whole-population occupation degrees $\langle O_s^{(I)} \rangle_r$ and $\langle O_w \rangle_r$ (for each realization, $O_s^{(I)} = \frac{1}{N_s} \sum_{i=1}^{N_s} O_i^{(I)}$ and $O_w = \frac{1}{N_s} \sum_{i=1}^{N_s} O_i^{(w)}$, and $\langle \dots \rangle_r$ denotes an average over realizations), the sub- and the whole-population pacing degrees $\langle P_s^{(I)} \rangle_r$ and $\langle P_w \rangle_r$ (for each realization, $P_s^{(I)} = \frac{1}{N_s} \sum_{i=1}^{N_s} P_i^{(I)}$ and $P_w = \frac{1}{N_s} \sum_{i=1}^{N_s} P_i^{(w)}$), and the statistical-mechanical sub- and whole-population spiking measures $M_s^{(I)}$ and $M_s^{(w)}$ for 18 values of J_{inter} in the sparsely synchronized region, and the results are shown in Figs. 7(a1)-7(c4). For the case of modular synchronization [occurring on the left region of the vertical dotted threshold line for $J_{inter} = J_{inter}^*$ ($\simeq 268$)], both the occupation degree $\langle O_w \rangle_r$ and the pacing degree $\langle P_w \rangle_r$ for the whole-population are less than those for the sub-populations because of mismatching between the intra-modular dynamics of sub-networks. As J_{inter} is increased, their mismatching degrees become smaller, and eventually $\langle O_w \rangle_r$ and $\langle P_w \rangle_r$ for the whole population become the same as those for the sub-populations for the case of global synchronization (occurring on the right region of the vertical dotted threshold line) due to perfect matching between the intra-modular dynamics of sub-networks. We first consider the occupation degree which characterizes the sparseness degree of population synchronization. For the sub-populations, the occupation degrees $\langle O_s^{(I)} \rangle_r$ decrease monotonically because of increase in inhibition with increasing J_{inter} . In the case of modular synchronization, typical IWPSR kernel estimates $R_w(t)$ show faster and smaller-amplitude oscillations with the whole-population frequency $f_p^{(w)}$ larger than the sub-population frequency $f_p^{(I)}$, and hence the occupation degree $\langle O_w \rangle_r$ for the whole-population becomes less than $\langle O_s^{(I)} \rangle_r$. As J_{inter} is increased, $\langle O_w \rangle_r$ increases and approaches $\langle O_s^{(I)} \rangle_r$ due to decrease in the mismatching degree between the intra-modular dynamics of sub-networks, and eventually when passing the threshold J_{inter}^* (i.e., in the case of global synchronization) they become the same and then decrease with increasing J_{inter} . We note that modular and global synchronization is sparse one because $\langle O_s^{(I)} \rangle_r$ is much less than unity [i.e., only a small fraction of the total L ($= 10^3$) neurons in the sub-population fire in each stripe]. Next, we consider the pacing degree between spikes in the stripes. For relatively small J_{inter} , with increasing J_{inter} the sub-population pacing degree $\langle P_s^{(I)} \rangle_r$ increases due to a constructive role of J_{inter} favoring the pacing between spikes, while for large J_{inter} $\langle P_s^{(I)} \rangle_r$ decreases as J_{inter} is increased because of a destructive role of J_{inter} spoiling the pacing between spikes. Through competition between these constructive and destructive roles of J_{inter} a “plateau”

with high pacing degree is formed in a relatively wide region of intermediate J_{inter} for the case of global sparse synchronization. The whole-population pacing degree $\langle P_w \rangle_r$ (which is less than or equal to $\langle P_s^{(I)} \rangle_r$) also exhibits similar behavior. Consequently, both the sub- and the whole-population statistical-mechanical spiking measures $M_s^{(I)}$ and $M_s^{(w)}$ (which are obtained by taking into consideration both the occupation and the pacing patterns of spikes in the stripes) show bell-shaped curves with their peaks at $J_{inter} \simeq 202$ (corresponding to modular sparse synchronization) and 287 (corresponding to global sparse synchronization), respectively. For further understanding of the pacing degree between spikes, we also consider the spatial cross-correlations between neuronal pairs. Figures 7(d1)-7(d5) show the spatial cross-correlation functions $C_l^{(I)}$ of Eq. (17) for $J_{inter} = 10, 30, 70, 400$, and 1200, respectively. For the case of relatively small J_{inter} , with increasing J_{inter} the value of $C_l^{(I)}$ increases, but it decreases for large J_{inter} . For quantitative analysis, we introduce the sub-population spatial cross-correlation degree $\langle \langle C_l^{(I)} \rangle_l \rangle_r$ given by double averaging of the spatial cross-correlation function $C_l^{(I)}$ over all lengths l and realizations. This sub-population spatial cross-correlation degree $\langle \langle C_l^{(I)} \rangle_l \rangle_r$ is a microscopic measure quantifying the cross-correlation degree between the microscopic IISR kernel estimates $r_i^{(I)}(t)$ without any explicit relation to the macroscopic occupation and pacing patterns of spikes. Figure 7(e) shows plots of $\langle \langle C_l^{(I)} \rangle_l \rangle_r$ versus J_{inter} for $I = 1, 2$, and 3. Similar to the case of the sub-population pacing degree $\langle P_s^{(I)} \rangle_r$, $\langle \langle C_l^{(I)} \rangle_l \rangle_r$ also display similar bell-shaped curves with peaks in the region of global synchronization. Hence, the statistical-mechanical pacing degree between spikes seems to be somewhat associated with the microscopic spatial cross-correlation degree between neuronal pairs.

In addition to the above study on the effect of J_{inter} along the route I for $M_{syn}^{(inter)} = 20$, we also investigate the effect of average number of inter-modular connections per interneuron $M_{syn}^{(inter)}$ on emergence of modular and global sparse synchronization along the routes II and III for $J_{inter} = 500$ and 2500, respectively [see Fig. 3(g)]. For the case of the route II with $J_{inter} = 500$, the raster plots of spikes in the three sub-populations for $M_{syn}^{(inter)} = 2, 5, 20$, and 50 are shown in Figs. 8(a1)-8(a4), respectively. The corresponding ISPSR and IWPSR kernel estimates, $R_s^{(I)}(t)$ and $R_w(t)$, for $M_{syn}^{(inter)} = 2, 5, 20$, and 50 are also shown in Figs. 8(b1)-8(b4), respectively. For each I th sub-population, sparse stripes are formed in the raster plot and the ISPSR kernel estimate $R_s^{(I)}(t)$ shows a regular oscillation. As $M_{syn}^{(inter)}$ is increased, more clear stripes appear in the raster plots of sub-networks, and hence

the amplitudes of $R_s^{(I)}(t)$ increase. Furthermore, with increasing $M_{syn}^{(inter)}$, the mismatching degree between the intra-modular dynamics of sub-networks decreases, and eventually when passing a threshold $M_{syn}^{(inter)*}$ ($\simeq 9$) perfect matching occurs. Figure 8(c) shows the plot of the cross-correlation modularity measure $\langle C_M \rangle_r$ of Eq. (19) versus $M_{syn}^{(inter)}$. Thus, for $M_{syn}^{(inter)} < M_{syn}^{(inter)*}$ modular sparse synchronization with $\langle C_M \rangle_r < 1$ emerges, while global sparse synchronization with $\langle C_M \rangle_r = 1$ appears for $M_{syn}^{(inter)} > M_{syn}^{(inter)*}$. In this way, with increasing $M_{syn}^{(inter)}$ the pacing degree between spikes increases monotonically thanks to the increase in the degree of effectiveness of global communication between spikes. Hence, $M_{syn}^{(inter)}$ plays only a constructive role to favor the pacing between spikes in sub-networks as well as the matching between the intra-modular dynamics of the sub-networks, in contrast to dual roles of J_{inter} for the case of route I. Hence, unsynchronization does not appear. This constructive role of $M_{syn}^{(inter)}$ may be seen explicitly in Figs. 8(d1)-8(f2). We first consider the occupation degree which characterizes the sparseness degree of spike synchronization. For the case of modular synchronization, the sub-population occupation degree $\langle O_s^{(I)} \rangle_r$ in the sub-networks decreases a little with increasing $M_{syn}^{(inter)}$, while $\langle O_s^{(I)} \rangle_r$ remains nearly constant for the case of global synchronization. On the other hand, as $M_{syn}^{(inter)}$ is increased the whole-population occupation degree $\langle O_w \rangle_r$ increases and approaches $\langle O_s^{(I)} \rangle_r$ because of decrease in the mismatching degree between the intra-modular dynamics of the sub-networks, and eventually when passing the threshold $M_{syn}^{(inter)*}$ they become the same and then remain nearly constant with increasing $M_{syn}^{(inter)}$. Hence, the constant behavior of $\langle O_s^{(I)} \rangle_r$ and $\langle O_w \rangle_r$ for the case of global synchronization (which may occur because the average inhibition given to each neuron is the same for constant inter-modular coupling strength, independently of $M_{syn}^{(inter)}$) is in contrast to the monotonically-decreasing behavior of $\langle O_s^{(I)} \rangle_r$ and $\langle O_w \rangle_r$ for the case of route I [refer to Figs. 7(a1)-7(a4)]. Since $\langle O_s^{(I)} \rangle_r < 1$ [i.e., only a small fraction of the total L ($= 10^3$) neurons in the sub-population fire in each stripe], modular and global synchronization is sparse one. Next, we consider the pacing degree between spikes in the stripes. For both cases of modular and global sparse synchronization, with increasing $M_{syn}^{(inter)}$ both the sub- and the whole-population pacing degrees $\langle P_s^{(I)} \rangle_r$ and $\langle P_w \rangle_r$ increase monotonically due to a constructive role of $M_{syn}^{(inter)}$ favoring the pacing between the spikes, in contrast to the bell-shaped behavior for the case of the route I [refer to Figs. 7(b1)-7(b4)]. Consequently, both the sub- and the whole-population statistical-mechanical spiking measures $M_s^{(I)}$ and $M_s^{(w)}$ (which are given by the products of the sub- and the whole-

population occupation and pacing degrees) increase monotonically in both cases of modular and global sparse synchronization, which is also in contrast to the case of the route I [refer to Figs. 7(c1)-7(c4)]. To further understand the pacing degree between spikes in the stripes, we consider the sub-population spatial cross-correlation degree $\langle\langle C_l^{(I)} \rangle_l\rangle_r$ between neuronal pairs [given by double averaging of the spatial cross-correlation function $C_l^{(I)}$ of Eq. (17) over all lengths l and realizations]. Figure 8(g) shows plots of $\langle\langle C_l^{(I)} \rangle_l\rangle_r$ versus $M_{syn}^{(inter)}$ for $I = 1, 2$, and 3 . Similar to the case of the sub-population pacing degree $\langle P_s^{(I)} \rangle_r$, $\langle\langle C_l^{(I)} \rangle_l\rangle_r$ also displays monotonic increasing behavior. Hence, the statistical-mechanical pacing degree between spikes seems to be associated with the microscopic spatial cross-correlation degree between neuronal pairs, like the case of route I.

We also investigate emergence of modular and global sparse synchronization by increasing $M_{syn}^{(inter)}$ along the route III for $J_{inter} = 2500$ (which is much larger than that for the case of route II). Unlike the case of the route II, for small $M_{syn}^{(inter)}$ a destructive effect to decrease the pacing degree between spikes occurs due to strong inhibition for $J_{inter} = 2500$, and hence when passing a lower threshold $M_{syn,l}^{(inter)*} (\simeq 6)$ a transition from modular sparse synchronization to unsynchronization occurs. However, with further increase in $M_{syn}^{(inter)}$ a constructive effect of $M_{syn}^{(inter)}$ to favor the pacing between spikes and the matching between the intra-modular dynamics of sub-networks overcomes the destructive effect of strong inhibition. Consequently, a transition to global sparse synchronization occurs when passing a higher threshold $M_{syn,h}^{(inter)*} (\simeq 26)$. These results are well shown in Figs. 9(a1)-9(h). The raster plots of spikes in the three sub-populations for $M_{syn}^{(inter)} = 1, 5, 20, 30$, and 50 are shown in Figs. 9(a1)-9(a5), respectively. The corresponding ISPSR and IWPSR kernel estimates, $R_s^{(I)}(t)$ and $R_w(t)$, for $M_{syn}^{(inter)} = 1, 5, 20, 30$, and 50 are also shown in Figs. 9(b1)-9(b5), respectively. For each I th sub-population, sparse stripes are formed in the raster plot and $R_s^{(I)}(t)$ shows a regular oscillation, except for the unsynchronized case of $M_{syn}^{(inter)} = 20$ where spikes are scattered without forming stripes in the raster plot and $R_s^{(I)}(t)$ is nearly stationary. Figures 9(c1)-9(c4) show the sub- and the whole-population order parameters $\mathcal{O}_s^{(I)}$ and \mathcal{O}_w which determine a threshold for the synchronization-unsynchronization transition. In the region of $M_{syn,l}^{(inter)*} < M_{syn}^{(inter)} < M_{syn,h}^{(inter)*}$, both $\mathcal{O}_s^{(I)}$ and \mathcal{O}_w tend to zero in the thermodynamic limit of $L \rightarrow \infty$, and hence unsynchronized states appear due to a destructive effect of strong inhibition. On the other hand, for $M_{syn}^{(inter)} < M_{syn,l}^{(inter)*}$ or $M_{syn}^{(inter)} > M_{syn,h}^{(inter)*}$, the values of $\langle\mathcal{O}_s^{(I)}\rangle_r$ and $\langle\mathcal{O}_w\rangle_r$ become saturated to non-zero limit values for large L , and hence

synchronized states exist. Particularly, for $M_{syn}^{(inter)} > M_{syn,h}^{(inter)*}$ sparsely synchronized states appear due to a constructive effect of $M_{syn}^{(inter)}$ favoring the pacing between spikes. The type of sparse synchronization may be determined in terms of the cross-correlation modularity measure C_M of Eq. (19) which is shown in Fig. 9(d). For $M_{syn}^{(inter)} < M_{syn,l}^{(inter)*}$ modular sparse synchronization with $\langle C_M \rangle_r < 1$ (i.e., some mismatching between the intra-modular dynamics of sub-networks) emerges, while global sparse synchronization with $\langle C_M \rangle_r = 1$ (i.e., perfect matching between the intra-modular dynamics of sub-networks) appears for $M_{syn}^{(inter)} > M_{syn,h}^{(inter)*}$. The degree of synchronization is also measured in terms of the occupation degrees, the pacing degrees, and the statistical-mechanical spiking measures in the sub- and the whole-populations, which are shown in Figs. 9(e1)-9(g2). We first consider the case of modular sparse synchronization. As M_{syn} is increased, both the occupation degree $\langle O_s^{(I)} \rangle_r$ and the pacing degree $\langle P_s^{(I)} \rangle_r$ in the sub-networks decrease due to a destructive effect of strong inhibition for $J_{inter} = 2500$. In the whole-population, with increasing M_{syn} the occupation degree $\langle O_w \rangle_r$ increases and approaches $\langle O_s^{(I)} \rangle_r$ because of decrease in the mismatching degree between the intra-modular dynamics of sub-networks, and the pacing degree $\langle P_w \rangle_r$ decreases like the case of $\langle P_s^{(I)} \rangle_r$. Thus, both the sub- and the whole-population statistical-mechanical spiking measures $M_s^{(I)}$ and $M_s^{(w)}$ (which are given by the products of the sub- and the whole-population occupation and pacing degrees) decrease as $M_{syn}^{(inter)}$ increases. On the other hand, for the case of global sparse synchronization which is similar to the case of route II, the constructive effect of $M_{syn}^{(inter)}$ favoring the pacing between spikes dominates. Consequently, with increasing $M_{syn}^{(inter)}$ both $\langle P_s^{(I)} \rangle_r$ and $\langle P_w \rangle_r$ increase monotonically, while both $\langle O_s^{(I)} \rangle_r$ and $\langle O_w \rangle_r$ remains nearly constant because the average inhibition given to each neuron is the same for constant inter-modular coupling strength J_{inter} , independently of $M_{syn}^{(inter)}$. Consequently, as $M_{syn}^{(inter)}$ is increased, the sub- and the whole-population statistical-mechanical spiking measures $M_s^{(I)}$ and $M_s^{(w)}$ show a monotonic increase. As in the case of route II, the modular and global synchronization is sparse one because $\langle O_s^{(I)} \rangle_r$ is much less than unity. Furthermore, the statistical-mechanical pacing degree between spikes in the sub-population seems to be associated with the spatial cross-correlation degree $\langle \langle C_l^{(I)} \rangle_l \rangle_r$ between neuronal pairs, which is shown in Fig. 9(h). For the case of modular sparse synchronization (i.e., $M_{syn}^{(inter)} < M_{syn,l}^{(inter)*}$), with increasing $M_{syn}^{(inter)}$ $\langle \langle C_l^{(I)} \rangle_l \rangle_r$ decreases monotonically due to a destructive role of strong inhibition, while for the case of global sparse synchronization (i.e., $M_{syn}^{(inter)} > M_{syn,h}^{(inter)*}$), $\langle \langle C_l^{(I)} \rangle_l \rangle_r$ exhibits a

monotonic increase because of a constructive role of $M_{syn}^{(inter)}$.

So far we studied the case 1 of intra-modular dynamics which are synchronized in the absence of inter-modular coupling in all identical sub-networks with $p_{rewiring} = 0.25$. From now on, we consider the 2nd case of the intra-modular dynamics which are unsynchronized in the absence of inter-modular coupling in all identical sub-networks with $p_{rewiring} = 0.05$. Figure 10 shows the state diagram in the J_{inter} - $M_{syn}^{(inter)}$ plane. This state diagram is similar to that for the case 1 in Fig. 3(g), except for the appearance of “L”-shaped region of unsynchronization. Modular and global sparse synchronization appears in the gray and the dark gray regions, respectively. Unsynchronization also occurs for large J_{inter} (> 1402) between the modular and the global synchronization. We investigate emergence of modular and global sparse synchronization by changing J_{inter} along the route of $M_{syn}^{(inter)} = 20$. Figures 11(a1)-11(a5) show the raster plots of spikes in the three sub-populations for $J_{inter} = 50, 200, 600, 1000$, and 2000 , respectively. The corresponding ISPSR and IWPSR kernel estimates, $R_s^{(I)}(t)$ and $R_w(t)$, for $J_{inter} = 50, 200, 600, 1000$, and 2000 are also shown in Figs. 11(b1)-11(b5), respectively. Unlike the case 1 of the intra-modular dynamics, for small J_{inter} ($=50$) unsynchronization occurs because of small $p_{rewiring}$ ($=0.05$). For this case, the clustering coefficient is high, and hence partial stripes (indicating local clustering of spikes) seem to appear in the raster plots of spikes. Thus, the raster plots show zigzag patterns intermingled with partial stripes with diverse inclinations and widths, and hence spikes become difficult to keep pace with each other. Consequently, $R_s^{(I)}(t)$ and $R_w(t)$ become nearly stationary. However, as J_{inter} is increased and passes a lower threshold $J_{inter,l}^*$ ($\simeq 187$), the inter-modular coupling strength J_{inter} plays a constructive role to favor the pacing between spikes in each sub-network, and synchronized states with regularly-oscillating $R_s^{(I)}(t)$ and $R_w(t)$ appear, as shown in the case of $J_{inter} = 200, 600$, and 1000 . On the other hand, for large J_{inter} , due to strong inhibition J_{inter} plays a destructive role to spoil the pacing between sparse spikes. Hence, when passing a higher threshold $J_{inter,h}^*$ ($\simeq 1402$), a transition to unsynchronization occurs, as shown for $J_{inter} = 2000$. For this case, sparse spikes in the raster plots in each sub-network are scattered without forming stripes, and hence both $R_s^{(I)}(t)$ and $R_w(t)$ become nearly stationary (i.e., every sub-network exhibits an unsynchronized state). Figures 11(c1)-11(c4) show the sub- and the whole-population order parameters $\mathcal{O}_s^{(I)}$ and \mathcal{O}_w which determine a threshold for the synchronization-unsynchronization transition. In the region of $J_{inter,l}^* < J_{inter} < J_{inter,h}^*$, the values of $\langle \mathcal{O}_s^{(I)} \rangle_r$ and $\langle \mathcal{O}_w \rangle_r$ become saturated to

non-zero limit values for large L , and hence synchronized states appear due to a constructive role of J_{inter} favoring the pacing between spikes. On the other hand, for $J_{inter} < J_{inter,l}^*$ or $J_{inter} > J_{inter,h}^*$ both $\langle O_s^{(I)} \rangle_r$ and $\langle O_w \rangle_r$ tend to zero in the thermodynamic limit of $L \rightarrow \infty$, and hence unsynchronized states appear. The type of sparse synchronization may be determined through calculation of the cross-correlation modularity measure C_M of Eq. (19). Figure 11(d) shows the plot of $\langle C_M \rangle_r$ versus J_{inter} . For $J_{inter,l}^* < J_{inter} < J_{inter}^*$ ($\simeq 451$) modular sparse synchronization with $\langle C_M \rangle_r < 1$ (i.e., some mismatching between the intra-modular dynamics of sub-networks) emerges, while global sparse synchronization with $\langle C_M \rangle_r = 1$ (i.e., perfect matching between the intra-modular dynamics of sub-networks) appears for $J_{inter}^* < J_{inter} < J_{inter,h}^*$. Figures 11(e1)-11(g2) show the average occupation degrees, the average pacing degrees, and the average statistical-mechanical spiking measures in the sub- and the whole-populations. In the synchronized region, their behaviors are similar to those for the case 1 [see Figs. 7(a1)-7(c4)]. We first consider the case of occupation degree characterizing the sparseness of spike synchronization in the synchronized region of $J_{inter,l}^* < J_{inter} < J_{inter,h}^*$. As J_{inter} is increased, the sub-population occupation degree $\langle O_s^{(I)} \rangle_r$ decreases monotonically due to increase in inhibition. In the whole-population, the occupation degree $\langle O_w \rangle_r$ for the case of modular synchronization becomes nearly saturated and approaches $\langle O_s^{(I)} \rangle_r$ because the modularity measure C_M between the sub-modular dynamics of sub-networks is relatively high and approaches unity, while $\langle O_w \rangle_r$ for the case of global synchronization with $\langle C_M \rangle_r = 1$ decreases monotonically along with $\langle O_s^{(I)} \rangle_r$. We also note that this modular and global synchronization is sparse one because $\langle O_s^{(I)} \rangle_r$ is much less than unity. Next, we consider the sub- and the whole-population pacing degrees $\langle P_s^{(I)} \rangle_r$ and $\langle P_w \rangle_r$ between spikes. With increasing J_{inter} , both $\langle P_s^{(I)} \rangle_r$ and $\langle P_w \rangle_r$ for relatively small J_{inter} increase due to a constructive role of J_{inter} to favor the pacing, while they decrease for large J_{inter} because of a destructive role of J_{inter} to spoil the pacing. For intermediate values of J_{inter} , a plateau with high pacing degrees is formed in each of $\langle P_s^{(I)} \rangle_r$ and $\langle P_w \rangle_r$. Thus, both the sub- and the whole-population statistical-mechanical spiking measures $M_s^{(I)}$ and $M_s^{(w)}$ (which are given by the products of the sub- and the whole-population occupation and pacing degrees) display bell-shaped behaviors. Figure 11(h) shows the plot of the spatial cross-correlation degree $\langle \langle C_l^{(I)} \rangle_l \rangle_r$ between neuronal pairs versus J_{inter} . Similar to the case of $\langle P_s^{(I)} \rangle_r$, $\langle \langle C_l^{(I)} \rangle_l \rangle_r$ also exhibits a bell-shaped curve with a plateau. Thus, $\langle P_s^{(I)} \rangle_r$ seem to be associated with $\langle \langle C_l^{(I)} \rangle_l \rangle_r$.

Finally, we consider the 3rd case of non-identical sub-networks where in the absence of inter-modular coupling, the 1st sub-network with $p_{rewiring} = 0.25$ is synchronized, the 2nd sub-network with $p_{rewiring} = 0.15$ is also synchronized, but the 3rd sub-network with $p_{rewiring} = 0.05$ is unsynchronized. Thanks to a constructive role of J_{inter} favoring the pacing between spikes, a transition to synchronization occurs in the 3rd sub-network when passing a lower threshold $J_{inter,l}^*$ for a given $M_{syn}^{(inter)}$ which are denoted by solid circles in Fig. 12(a). With increasing $M_{syn}^{(inter)}$, the value of $J_{inter,l}^*$ decreases due to a constructive effect of $M_{syn}^{(inter)}$ to favor the pacing between spikes. For $J < J_{inter,l}^*$, the 3rd sub-network is still unsynchronized, while the 1st and the 2nd sub-systems are synchronized. As J_{inter} passes $J_{inter,l}^*$, the 3rd sub-network becomes synchronized, and then modular synchronization occurs due to mismatching between the intra-modular dynamics of sub-networks. Here, we consider the case of $J_{inter} > J_{inter,l}^*$. Figure 12(b) shows the state diagram in the J_{inter} - $M_{syn}^{(inter)}$ plane for the case of $J_{inter} \geq 1$ and $M_{syn}^{(inter)} \geq 1$ (i.e., the region where the 1st and the 2nd sub-networks are synchronized but the 3rd sub-network is unsynchronized is not shown). We note that this state diagram is nearly the same as that for the case 1 in Fig. 3(g). Modular sparse synchronization occurs in the “L”-shaped gray region, while global synchronization appears in the dark gray region. Unsynchronization also occurs for large J_{inter} (> 1371) between modular and global synchronization. When compared with the case 1 of the intra-modular dynamics [see Fig. 3(g)], the regions of modular synchronization and unsynchronization are a little enlarged, while the region of global synchronization is somewhat contracted. We study appearance of modular and global synchronization by increasing J_{inter} from the threshold $J_{inter,l}^*(\simeq 0.2)$ for the 3rd sub-network along the route of $M_{syn}^{(inter)} = 20$. Figures 13(a1)-13(a5) show the raster plots of spikes in the three sub-networks for $J_{inter} = 10, 100, 500, 1000$, and 2000 , respectively. The ISPSR and IWPSR kernel estimates, $R_s^{(I)}(t)$ and $R_w(t)$, for $J_{inter} = 10, 100, 500, 1000$, and 2000 are also shown in Figs. 13(b1)-13(b5), respectively. For $J_{inter} = 10$, due to a constructive role of J_{inter} favoring the pacing between spikes, sparse stripes are formed in each I th sub-population ($I = 1, 2, 3$). However, in contrast to the case 1 of identical intra-modular dynamics, the smearing degree of stripes is different, depending on the sub-population [compare Fig. 13(a1) with Fig. 6(a1)]. The stripes for the 1st sub-population (with $p_{rewiring} = 0.25$) are relatively clear, while the stripes in the other 2nd and 3rd sub-populations (with $p_{rewiring} = 0.15$ and 0.05 , respectively) are more and more smeared. Hence, the amplitudes of the regularly-

oscillating $R_s^{(I)}(t)$ decrease as I is increased. As J_{inter} is further increased (e.g., see the cases of $J_{inter}=100$ and 500), the pacing degree of spikes in the stripes increases for each sub-population, although the stripes become more sparse. However, for large J_{inter} (e.g., $J_{inter} = 1000$), due to a destructive role of J_{inter} the pacing degree of spikes in the stripes begins to decrease. Eventually, when passing a higher threshold $J_{inter,h}^*$ ($\simeq 1372$) a transition to unsynchronization occurs. Thus, for $J_{inter} = 2000$, spikes are scattered in the raster plot, and both $R_s^{(I)}(t)$ and $R_w(t)$ are nearly stationary. Figures 13(c1)-13(c4) show the sub- and the whole-population order parameters $\langle \mathcal{O}_s^{(I)} \rangle_r$ and $\langle \mathcal{O}_w \rangle_r$ which determine a threshold for the synchronization-unsynchronization transition. For $J_{inter,l}^* (\simeq 0.2) < J_{inter} < J_{inter,h}^* (\simeq 1372)$, synchronized states exist because the values of $\langle \mathcal{O}_s^{(I)} \rangle_r$ and $\langle \mathcal{O}_w \rangle_r$ approach non-zero limit values for large L . On the other hand, when passing the higher threshold $J_{inter,h}^*$, a transition to unsynchronization occurs because the order parameters $\langle \mathcal{O}_s^{(I)} \rangle_r$ and $\langle \mathcal{O}_w \rangle_r$ tend to zero as $L \rightarrow \infty$. These unsynchronized states seem to appear due to a destructive effect of strong inhibition spoiling the pacing between sparse spikes. In the synchronized region of $J_{inter,l}^* < J_{inter} < J_{inter,h}^*$, the type of sparse synchronization may be determined by calculating the cross-correlation modularity measure C_M of Eq. (19). Figure 13(d) shows the plot of $\langle C_M \rangle_r$ versus J_{inter} . For $J_{inter,l}^* < J_{inter} < J_{inter}^*$ ($\simeq 357$), modular sparse synchronization with $\langle C_M \rangle_r < 1$ (i.e., some mismatching between the intra-modular dynamics of the sub-networks) appears, while global sparse synchronization with $\langle C_M \rangle_r = 1$ (i.e., perfect matching between the intra-modular dynamics of the sub-networks) emerges for $J_{inter}^* < J_{inter} < J_{inter,h}^*$. We also measure the degree of modular and global synchronization in terms of realistic sub- and whole-population statistical-mechanical spiking measures. Figures 13(e1)-13(g2) show the average occupation degrees, the average pacing degrees, and the average statistical-mechanical spiking measures in the sub- and the whole-populations. Their behaviors are similar to those for the case 1 [see Figs. 7(a1)-7(c4)]. We first consider the case of occupation degree which characterizes the sparseness of spike synchronization. As J_{inter} is increased from $J_{inter,l}^*$, all the sub-population occupation degrees $\langle \mathcal{O}_s^{(I)} \rangle_r$ are nearly the same and decrease monotonically due to increase in inhibition. In the case of modular synchronization, with increasing J_{inter} the occupation degree $\langle \mathcal{O}_w \rangle_r$ for the whole-population increases and approaches $\langle \mathcal{O}_s^{(I)} \rangle_r$ due to decrease in the mismatching degree between the intra-modular dynamics of sub-populations, and eventually when passing the threshold J_{inter}^* (i.e., in the case of global synchronization) they become the same and then decrease together as J_{inter} is

increased. This modular and global synchronization is sparse one because $\langle O_s^{(I)} \rangle_r < 1$. Next, we consider the sub- and the whole-population pacing degrees $\langle P_s^{(I)} \rangle_r$ and $\langle P_w \rangle_r$ between spikes. For the case of modular synchronization, $\langle P_s^{(1)} \rangle_r > \langle P_s^{(2)} \rangle_r > \langle P_s^{(3)} \rangle_r$, unlike the case 1 of intra-modular dynamics of case 1 [compare Fig. 13(f1) with Figs. 7(b1)-7(b3)]. As J_{inter} is increased from $J_{inter,l}^*$ each sub-population pacing degree $\langle P_s^{(I)} \rangle_r$ increases independently and approaches each other due to a constructive role of J_{inter} to favor the pacing between spikes. Eventually, when passing the threshold J_{inter}^* (i.e., for the case of global synchronization) these sub-population pacing degrees $\langle P_s^{(I)} \rangle_r$ become the same, and then a plateau with high pacing degree is formed in $\langle P_s^{(I)} \rangle_r$. With further increase in J_{inter} , $\langle P_s^{(I)} \rangle_r$ decreases because of a destructive role of J_{inter} to spoil the pacing between spikes. Similar to $\langle P_s^{(I)} \rangle_r$, the whole-population pacing degree $\langle P_w \rangle_r$ also displays a bell-shaped curve. Consequently, both the sub- and the whole-population statistical-mechanical spiking measures $M_s^{(I)}$ and $M_s^{(w)}$ (which are given by the products of the sub- and the whole-population occupation and pacing degrees) exhibit bell-shaped behaviors. Figure 13(h) shows the plots of the sub-population spatial cross-correlation degrees $\langle \langle C_l^{(I)} \rangle_l \rangle_r$ between neuronal pairs versus J_{inter} . Similar to the case of $\langle P_s^{(I)} \rangle_r$, each $\langle \langle C_l^{(I)} \rangle_l \rangle_r$ also exhibits a bell-shaped curve; in the case of modular synchronization they increase independently and approach each other, and eventually for the case of global synchronization they become the same, which is also in contrast to the case 1 of intra-modular dynamics [compare Fig. 13(h) with Fig. 7(e)]. Thus, $\langle P_s^{(I)} \rangle_r$ also seems to be associated with $\langle \langle C_l^{(I)} \rangle_l \rangle_r$.

IV. SUMMARY

In order to extend previous works on sparse synchronization in non-modular networks [13–18, 60, 61] to the case of modular networks, we investigated the effect of inter-modular connection on emergence of sparsely synchronized cortical rhythms, which are associated with diverse cognitive functions, in clustered small-world networks of inhibitory FS interneurons. In the absence of inter-modular coupling, we considered three cases for the intra-modular dynamics in the sub-networks: (1) synchronized in all identical sub-networks, (2) unsynchronized in all identical sub-networks, and (3) synchronized/unsynchronized in non-identical sub-networks. For each case, we studied emergence of sparsely synchronized population states by varying both the inter-modular coupling strength J_{inter} and the average

number of inter-modular links per interneuron $M_{syn}^{(inter)}$. Consequently, two kinds of sparse synchronization such as modular and global synchronization have been found, in contrast to the case of non-clustered networks. For the case of modular sparse synchronization, the population behavior reveals the modular structure due to some mismatching between the intra-modular dynamics of sub-networks, while in the case of global sparse synchronization, the population behavior is globally identical, independently of the cluster structure, because of perfect matching between the intra-modular dynamics of sub-networks. We introduced a realistic cross-correlation modularity measure, representing the matching-degree between the ISPSR kernel estimates $R_s^{(I)}(t)$ of the sub-networks, and examined whether the sparse synchronization is global or modular. Through this study, it has been found that the inter-modular coupling strength J_{inter} seems to play dual roles for the pacing between spikes in each sub-network, depending on its magnitude. For large J_{inter} it plays a destructive role to spoil the pacing between sparse spikes, and hence when passing a large threshold, a transition to unsynchronization occurs due to strong inhibition. On the other hand, for small J_{inter} it plays a constructive role to favor the pacing between spikes in each sub-network. Through competition between these constructive and destructive roles of J_{inter} , there appears an intermediate optimal J_{inter} at which the pacing degree between spikes becomes maximal. In contrast, the average number of inter-modular connections per interneuron $M_{syn}^{(inter)}$ plays a role just favoring the pacing between spikes. As $M_{syn}^{(inter)}$ is increased, the degree of effectiveness of global communication between spikes increases, which results in the monotonic increase in the pacing degree. We have also determined the threshold values for the synchronization-unsynchronization transitions in the sub- and whole-populations by employing the realistic sub- and whole-population order parameters, based on the IWPSR kernel estimate $R_w(t)$ and the ISPSR kernel estimate $R_s^{(I)}(t)$. Furthermore, the degrees of modular and global sparse synchronization have also been measured in terms of the realistic sub- and whole-population statistical-mechanical spiking measures defined by considering both the occupation and the pacing degrees of the spikes. The statistical-mechanical pacing degree between spikes has also been found to be associated with the microscopic spatial cross-correlation degree between neuronal pairs. Finally, we expect that our results on the inter-modular connection effect in modular networks have important implications for the role of the brain plasticity which refers to the brain's ability to change its structure and function by modifying structure and strength of synaptic connections during the development [82].

Acknowledgments

This research was supported by Basic Science Research Program through the National Research Foundation of Korea(NRF) funded by the Ministry of Education (Grant No. 2013057789).

- [1] G. Buzsáki, *Rhythms of the Brain* (Oxford University Press, New York, 2006).
- [2] R. D. Traub and M. A. Whittington, *Cortical Oscillations in Health and Diseases* (Oxford University Press, New York, 2010).
- [3] X.-J. Wang, *Physiol. Rev.* **90**, 1195 (2010).
- [4] E. H. Buhl, G. Tamas, and A. Fisahn, *J. Physiol.* **513**, 117 (1998).
- [5] A. Fisahn, F. G. Pike, E. H. Buhl, and O. Paulsen, *Nature* **394**, 186 (1998).
- [6] J. Csicsvari, H. Hirase, A. Czurko, and G. Buzsáki, *Neuron* **21**, 179 (1998).
- [7] J. Csicsvari, H. Hirase, A. Czurko, A. Mamiya, and G. Buzsáki, *J. Neurosci.* **19**, 274 (1999).
- [8] J. Fellous and T. J. Sejnowski, *Hippocampus* **10**, 187 (2000).
- [9] P. Fries, J. H. Reynolds, A.E. Rorie, and R. Desimone, *Science* **291**, 1560 (2001).
- [10] N. K. Logothetis, J. Pauls, M. A. Augath, T. Trinath, and A. Oeltermann, *Nature* **412**, 150 (2001).
- [11] X.-J. Wang and G. Buzsáki, *J. Neurosci.* **16**, 6402 (1996).
- [12] X.-J. Wang, in *Encyclopedia of Cognitive Science*, edited by L. Nadel (MacMillan, London, 2003), pp. 272-280.
- [13] N. Brunel and V. Hakim, *Neural Comput.* **11**, 1621 (1999).
- [14] N. Brunel, *J. Comput. Neurosci.* **8**, 183 (2000).
- [15] N. Brunel and X.-J. Wang, *J. Neurophysiol.* **90**, 415 (2003).
- [16] C. Geisler, N. Brunel, and X.-J. Wang, *J. Neurophysiol.* **94**, 4344 (2005).
- [17] N. Brunel and D. Hansel, *Neural Comp.* **18**, 1066 (2006).
- [18] N. Brunel and V. Hakim, *Chaos* **18**, 015113 (2008).
- [19] W. Lim and S.-Y. Kim, *J. Comput. Neurosci.* **31**, 667 (2011).
- [20] D.-G. Hong, S.-Y. Kim, and W. Lim, *J. Korean Phys. Soc.* **59**, 2840 (2011).
- [21] S.-Y. Kim and W. Lim, *J. Korean Phys. Soc.* **63**, 104 (2013).

- [22] O. Sporns, *Networks of the Brain* (MIT Press, Cambridge, 2011).
- [23] G. Buzsáki, C. Geisler, D.A. Henze, and X.-J. Wang, *Trends in Neurosciences* **27**, 186 (2004).
- [24] D.B. Chklovskii, B.W. Mel, and K. Svoboda, *Nature* **431**, 782 (2004).
- [25] S. Song, P.J. Sjöström, M. Reigl, S. Nelson, and D. B. Chklovskii, *PLoS Biol.* **3**, e68 (2005).
- [26] O. Sporns and C.J. Honey, *Proc. Natl. Acad. Sci. USA* **103**, 19219 (2006).
- [27] P. Larimer and B.W. Strowbridge, *J. Neurosci.* **28**, 12212 (2008).
- [28] E. Bullmore and O. Sporns, *Nat. Rev. Neurosci.* **10**, 186 (2009).
- [29] O. Sporns, G. Tononi, and G.M. Edelman, *Cereb. Cortex* **10**, 127 (2000).
- [30] D. S. Bassett and E. Bullmore, *The Neuroscientist* **12**, 512 (2006).
- [31] C. C. Hilgetag, G. A. P. C. Burns, M. A. O'Neill, J. W. Scannell, and M. P. Young, *Phil. Trans. R. Soc. Lond. B* **355**, 91 (2000).
- [32] C. C. Hilgetag and M. Kaiser, *Neuroinformatics* **2**, 353 (2004).
- [33] O. Sporns, D. Chialvo, M. Kaiser, and C. Hilgetag, *Trends Cogn. Sci.* **8**, 418 (2004).
- [34] S.-J. Wang, C. C. Hilgetag, and C. S. Zhou, *Front. Comput. Neurosci.* **5**, 30 (2011).
- [35] L. Zemanová, C. S. Zhou, and J. Kurths, *Physica D* **224**, 202 (2006).
- [36] C. S. Zhou, L. Zemanová, G. Zamora-López, C.-C. Hilgetag, and J. Kurths, *Phys. Rev. Lett.* **97**, 238103 (2006).
- [37] C. Zhou, L. Zemanová, G. Zamora-López, C. Hilgetag, and J. Kurths, *New J. Phys.* **9**, 178 (2007).
- [38] G. Zamora-López, C. Zhou, and J. Kurths, *Chaos* **19**, 015117 (2009).
- [39] G. Zamora-López, C. Zhou, and J. Kurths, *Front. Neuroinf.* **4**, 1 (2010).
- [40] G. Zamora-López, C. Zhou, and J. Kurths, *Front. Neurosci.* **5**, 83 (2011).
- [41] O. Sporns, C. J. Honey, and R. Kötter, *PLoS ONE* **2**, e1049 (2007).
- [42] P. Hagmann, L. Cammoun, X. Gigandet, R. Meuli, C. J. Honey, V. J. Wedeen, and O. Sporns, *PLoS Biol.* **6**, e159 (2008).
- [43] D.J. Watts and S.H. Strogatz, *Nature* **393**, 440 (1998).
- [44] S. H. Strogatz, *Nature* **410**, 268 (2001).
- [45] D. J. Watts, *Small Worlds: The Dynamics of Networks Between Order and Randomness* (Princeton University Press, 2003).
- [46] S. Milgram, *Psychology Today* **1**, 61 (1967).
- [47] J. Guare, *Six Degrees of Separation: A Play* (Random House, New York, 1990).

- [48] L.F. Lago-Fernández, R. Huerta, F. Corbacho, and J.A. Sigüenza, Phys. Rev. Lett. **84**, 2758 (2000).
- [49] O. Kwon and H. T. Moon, Phys. Lett. A **298**, 319 (2002).
- [50] A. Roxin, H. Riecke, and S.A. Solla, Phys. Rev. Lett. **92**, 198101 (2004).
- [51] M. Kaiser and C. C. Hilgetag, PLoS Comp. Biol. **2**, e95 (2006).
- [52] H. Riecke, A. Roxin, S. Madruga, and S. Solla, Chaos **17**, 026110 (2007).
- [53] S. Achard and E.T. Bullmore, PLoS Comp. Biol. **3**, e17 (2007).
- [54] S. Yu, D. Huang, W. Singer, and D. Nikolic, Cereb. Cortex **18**, 2891 (2008).
- [55] Q. Wang, Z. Duan, M. Perc, and G. Chen, Europhys. Lett. **83**, 50008 (2008).
- [56] M. Shanahan, Phys. Rev. E **78**, 041924 (2008).
- [57] M. Ozer, M. Perc, and M. Uzuntarla, Phys. Lett. A **373**, 964 (2009).
- [58] Q. Wang, M. Perc, Z. Duan, and G. Chen, Physica A **389**, 3299 (2010).
- [59] J.T. Lizier, S. Pritam, and M. Prokopenko, Artificial Life **17**, 293 (2011).
- [60] S.-Y. Kim and W. Lim, Physica A **421**, 109 (2015).
- [61] S.-Y. Kim and W. Lim (accepted for publication in Phys. Rev. E; e-print:arXiv:1504.03063 [q-bio.NC]).
- [62] X. Sun, J. Lai, M. Perc, J. Kurths, and G. Chen, Chaos **21**, 016110 (2011).
- [63] C. A. S. Batista, E. L. Lameu, A. M. Batista, S. R. Lopes, T. Pereira, G. Zamora-López, J. Kurths, and R. L. Viana, Phys. Rev. E **86**, 016211 (2012).
- [64] H.-T. Yu, J. Wang, B. Deng, and X.-L. Wei, Chin. Phys. B **22**, 018701 (2013).
- [65] E. L. Lameu, C. A. S. Batista, A. M. Batista, K. Iarosz, R. L. Viana, S. R. Lopes, and J. Kurths, Chaos **22**, 043149 (2012).
- [66] S.-Y. Kim and W. Lim, J. Neurosci. Methods **226**, 161 (2014).
- [67] E. M. Izhikevich, IEEE Trans. Neural Networks **14**, 1569 (2003).
- [68] E. M. Izhikevich, IEEE Trans. Neural Networks **15**, 1063 (2004).
- [69] E. M. Izhikevich, *Dynamical Systems in Neuroscience* (MIT Press, Cambridge, 2007).
- [70] E. M. Izhikevich, Trans. R. Soc. A **368**, 5061 (2010).
- [71] A. L. Hodgkin, J. Physiol. **107**, 165 (1948).
- [72] E. M. Izhikevich, Int. J. Bif. Chaos **10**, 1171 (2000).
- [73] M. San Miguel and R. Toral, in *Instabilities and Nonequilibrium Structures VI*, edited by J. Martinez, R. Tiemann, and E. Tirapegui (Kluwer Academic Publisher, Dordrecht, 2000), p.

- [74] H. Shimazaki and S. Shinomoto, J. Comput. Neurosci. **29**, 171 (2010).
- [75] D. Golomb and J. Rinzel, Physica D **72**, 259 (1994).
- [76] A. Longtin, Nuovo Cimento D **17**, 835 (1995).
- [77] A. Longtin, in *Stochastic Dynamics and Pattern Formation in Biological and Complex Systems*, edited by S. Kim, K. J. Lee, and W. Sung (AIP, New York, 2000), pp. 219-239.
- [78] D. Hansel and G. Mato, Neural Comput. **15**, 1 (2003).
- [79] D. Hansel and H. Sompolinsky, Phys. Rev. Lett. **68**, 718 (1992).
- [80] I. Ginzburg and H. Sompolinsky, Phys. Rev. E **50**, 3171 (1994).
- [81] J. Freund, L. Schimansky-Geier, and P. Hänggi, Chaos **13**, 225 (2003).
- [82] A. Pascual-Leone, C. Freitas, L. Oberman, J.C. Horvath, M. Halko, M. Eldaief, S. Bashir, M. Vernet, M. Shafi, B. Westover, A.M. Vahabzadeh-Hagh, and A. Rotenberg, Brain Topography **24**, 302 (2011).

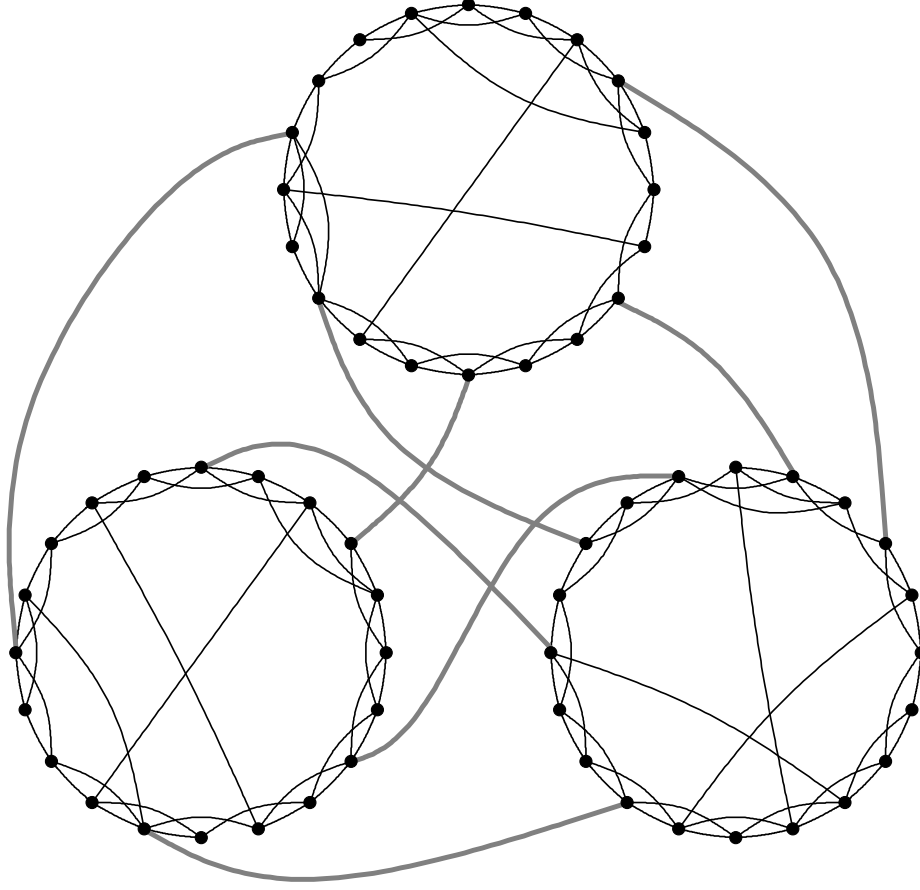


FIG. 1: Schematic representation of the clustered small-world network topology. The whole network consists of $M(= 3)$ Watts-Strogatz small-world sub-networks, each of them containing $L(= 20)$ interneurons. Within each sub-network, the average number of intra-modular synaptic inputs per interneuron is $M_{syn}^{(intra)}(= 4)$, while there are 8 sparse random inter-modular connections (denoted by heavy lines) between the sub-networks.

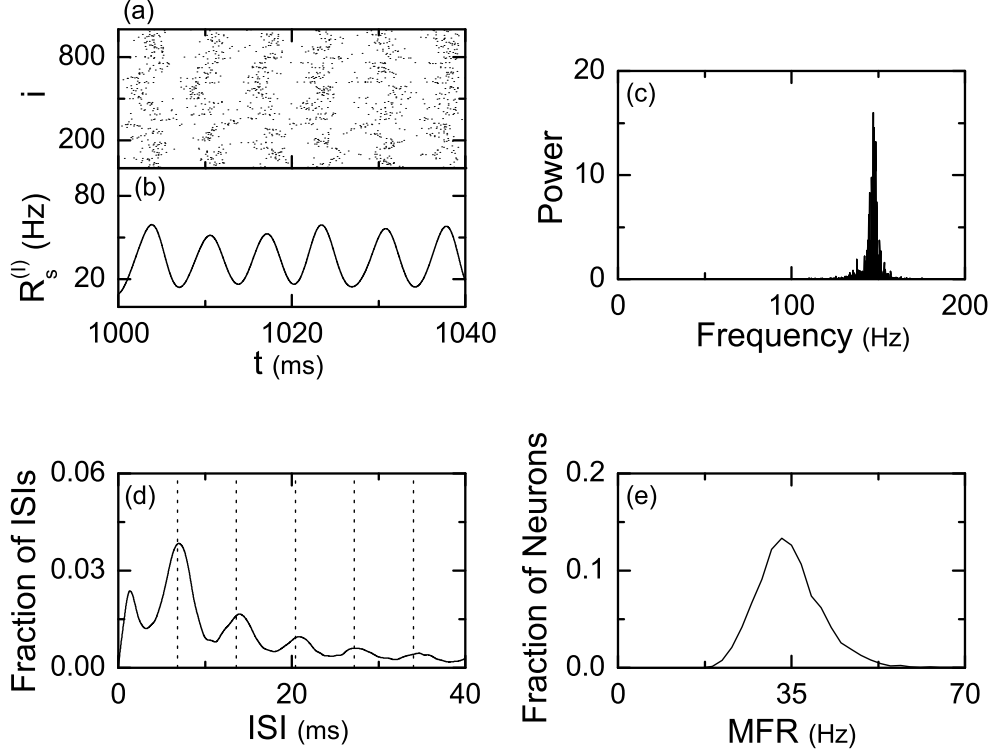


FIG. 2: Fast sparse synchronization in each small-world sub-network of $L(= 10^3)$ FS Izhikevich interneurons in the absence of inter-modular coupling for $I_{DC} = 1500$, $D = 500$, $M_{syn}^{(intra)} = 50$, $p_{rewiring} = 0.25$, and $J_{intra} = 1400$. (a) Raster plot of neural spikes and (b) instantaneous sub-population spike rate kernel estimate $R_s^{(I)}(t)$; the band width of the Gaussian kernel estimate is $h = 1$ ms. (c) One-sided power spectrum of $\Delta R_s^{(I)}(t) [= R_s^{(I)}(t) - \overline{R_s^{(I)}(t)}]$ with the mean-squared amplitude normalization. The number of data for the power spectrum is 2^{13} , and the overline denotes the time average. (d) Inter-spike interval (ISI) histogram for the individual interneurons. The ISI histogram is composed of 5×10^4 ISIs, the bin size for the histogram is 0.5 ms, and the vertical dotted lines denote integer multiples of the global period T_I ($\simeq 6.8$ ms) of $R_s^{(I)}(t)$. (e) MFR (mean firing rate) distribution of individual interneurons. The MFR for each interneuron is calculated by following the membrane potential during the averaging time of 2×10^4 ms after discarding the transient time of 10^3 ms, and the bin size is 2 Hz.

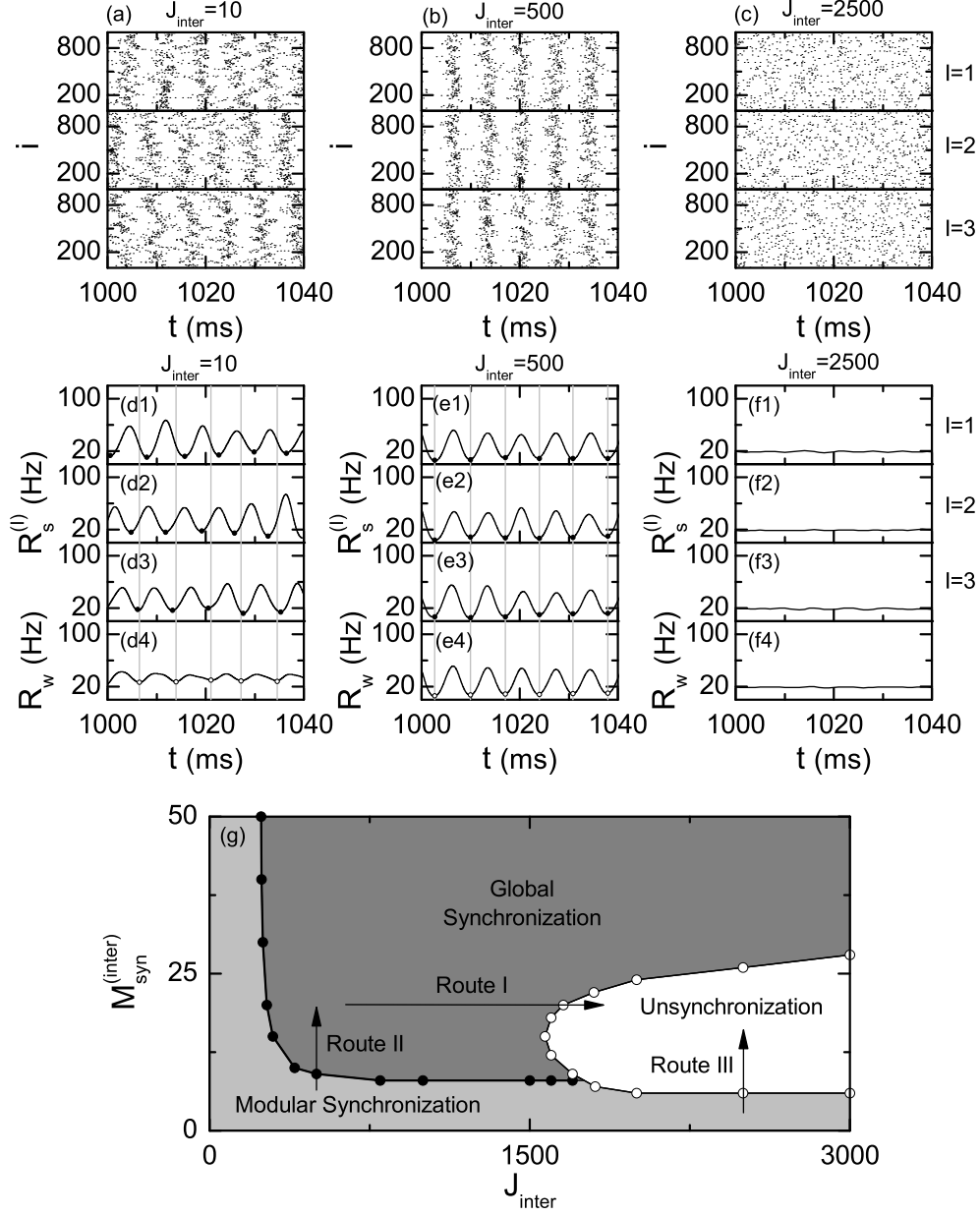


FIG. 3: Modular and global sparse synchronization in the clustered network with 3 small-world sub-networks, each of them containing $L(= 10^3)$ FS Izhikevich interneurons in the case of $I_{DC} = 1500$, $D = 500$, $M_{syn}^{(intra)} = 50$, $p_{rewiring} = 0.25$, and $J_{intra} = 1400$. $M_{syn}^{(inter)} = 20$ in (a)-(f4). Raster plots of neural spikes in the sub-networks ($I = 1, 2, 3$): (a) modular sparse synchronization for $J_{inter} = 10$, (b) global sparse synchronization for $J_{inter} = 500$, and (c) unsynchronization for $J_{inter} = 2500$. Instantaneous sub- and whole-population spike rate kernel estimates, $R_s^{(I)}(t)$ ($I = 1, 2, 3$) and $R_w(t)$: (d1)-(d4) modular sparse synchronization for $J_{inter} = 10$, (e1)-(e4) global sparse synchronization for $J_{inter} = 500$, and (f1)-(f4) unsynchronization for $J_{inter} = 2500$; the band width of the Gaussian kernel estimate is $h = 1$ ms. Vertical gray lines for $J_{inter} = 10$ and 500 pass minima of $R_w(t)$, and the minima of $R_s^{(I)}(t)$ [$R_w(t)$] are denoted by solid (open) circles. (g) State diagram in the J_{inter} - $M_{syn}^{(inter)}$ plane.

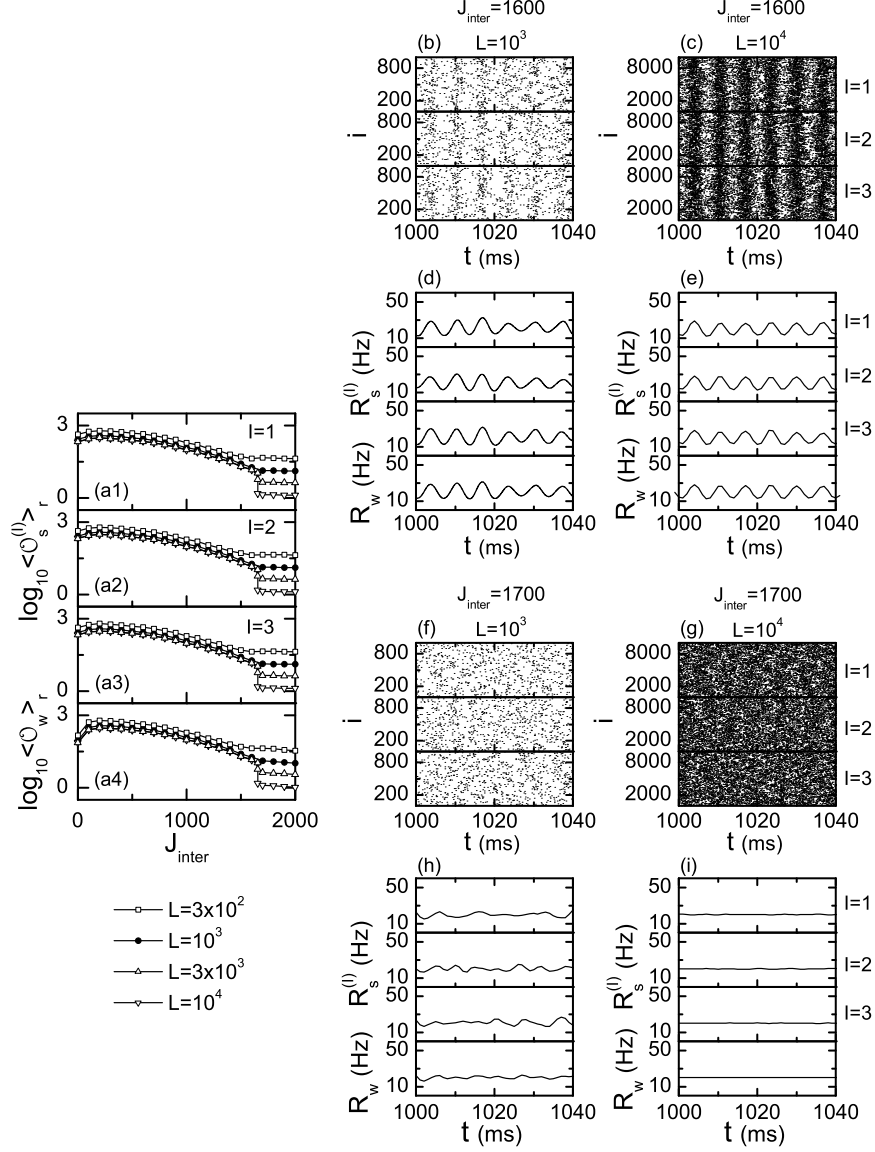


FIG. 4: Realistic thermodynamic order parameters for measurement of the threshold for the synchronization-unsynchronization transition in the clustered network with 3 small-world sub-networks, each of them containing L FS Izhikevich interneurons for $M_{syn}^{(inter)} = 20$ [route I in Fig. 3(g)] in the case of $I_{DC} = 1500$, $D = 500$, $M_{syn}^{(intra)} = 50$, $p_{rewiring} = 0.25$, and $J_{intra} = 1400$. (a1)-(a4) Plots of the sub- and the whole-population order parameters $\log_{10} \mathcal{O}_s^{(I)}$ ($I = 1, 2, 3$) and $\log_{10} \mathcal{O}_w$ versus J_{inter} . For each J_{inter} , the order parameter is obtained through average over 20 realizations, and the averaging time for the calculation of the order parameter in each realization is 4×10^3 ms. Sparse synchronization for $J_{inter} = 1600$: raster plots of neural spikes in the three sub-networks for (b) $L = 10^3$ and (c) $L = 10^4$ and instantaneous sub- and whole-population spike rate kernel estimates $R_s^{(I)}(t)$ ($I = 1, 2, 3$) and $R_w(t)$ for (d) $L = 10^3$ and (e) $L = 10^4$. Unsynchronization for $J_{inter} = 1700$: raster plots of neural spikes in the three sub-networks for (f) $L = 10^3$ and (g) $L = 10^4$ and instantaneous sub- and whole-population spike rate kernel estimates $R_s^{(I)}(t)$ ($I = 1, 2, 3$) and $R_w(t)$ for (h) $L = 10^3$ and (i) $L = 10^4$. The band width of the Gaussian kernel estimate is $h = 1$ ms.

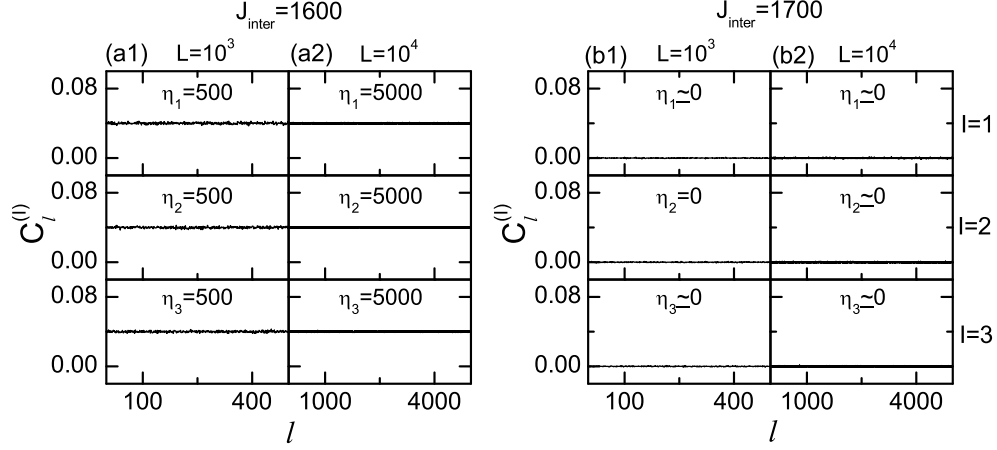


FIG. 5: Spatial cross-correlation functions for the synchronized and the unsynchronized states in the clustered network with 3 small-world sub-networks, each of them containing L FS Izhikevich interneurons for $M_{syn}^{(inter)} = 20$ [route I in Fig. 3(g)] in the case of $I_{DC} = 1500$, $D = 500$, $M_{syn}^{(intra)} = 50$, $p_{rewiring} = 0.25$, and $J_{intra} = 1400$. Sparse synchronization for $J_{inter} = 1600$ with the spatial correlation length η_I covering the whole sub-network: spatial cross-correlation functions $C_l^{(I)}$ in the three sub-networks ($I = 1, 2, 3$) for (a1) $L = 10^3$ and (a2) $L = 10^4$. Unsynchronization for $J_{inter} = 1700$ with $\eta_I \simeq 0$: spatial cross-correlation functions $C_l^{(I)}$ in the three sub-networks for (b1) $L = 10^3$ and (b2) $L = 10^4$. For each J_{inter} , the number of data used for the calculation of each temporal cross-correlation function $C_{i,j}^{(I)}(\tau)$ is 4×10^3 .

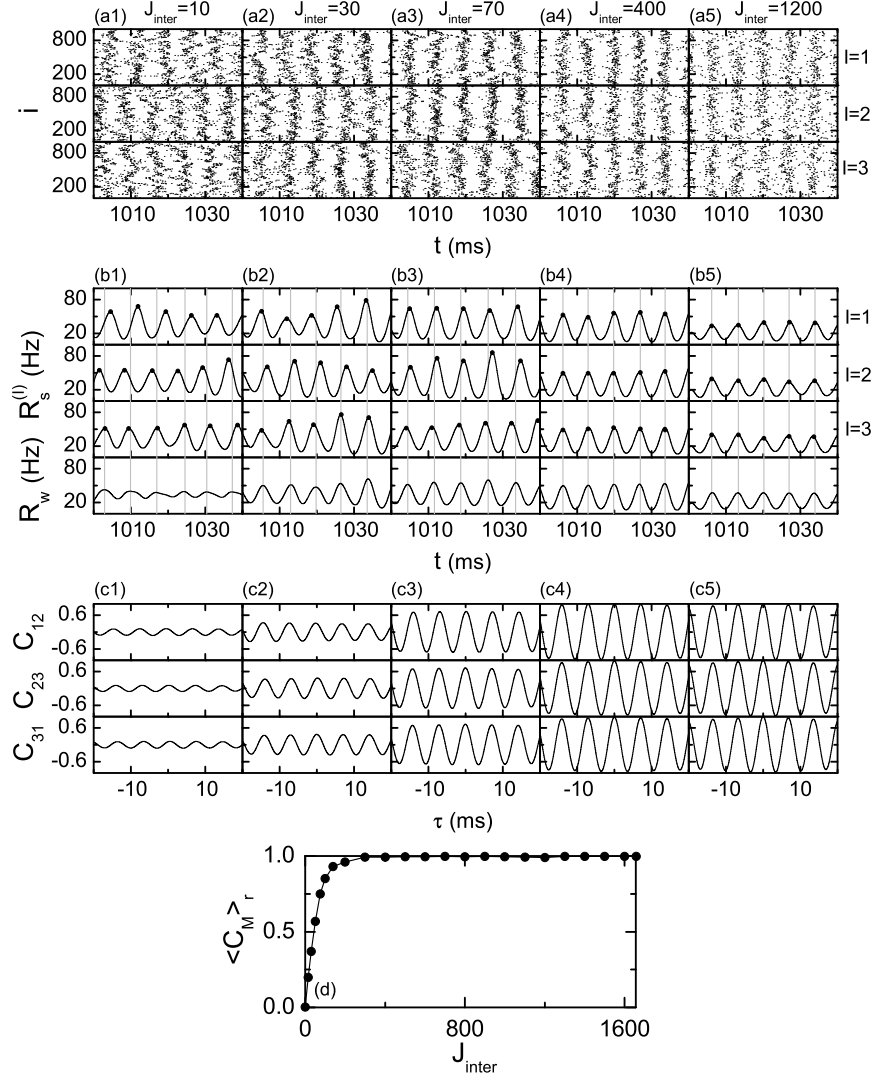


FIG. 6: Realistic cross-correlation modularity measure for determining the threshold for modular-global sparse synchronization transition in the clustered network with 3 small-world sub-networks, each of them containing $L(= 10^3)$ FS Izhikevich interneurons for $M_{syn}^{(inter)} = 20$ [route I in Fig. 3(g)] in the case of $I_{DC} = 1500$, $D = 500$, $M_{syn}^{(intra)} = 50$, $p_{rewiring} = 0.25$, and $J_{intra} = 1400$. Raster plots of neural spikes in the sub-networks ($I = 1, 2, 3$): modular sparse synchronization for $J_{inter} =$ (a1) 10, (a2) 30, and (a3) 70, and global sparse synchronization for $J_{inter} =$ (a4) 400 and (a5) 1200. Instantaneous sub- and whole-population spike rate kernel estimates $R_s^{(I)}$ ($I = 1, 2, 3$) and $R_w(t)$: modular sparse synchronization for $J_{inter} =$ (b1) 10, (b2) 30, and (b3) 70, and global sparse synchronization for $J_{inter} =$ (b4) 400 and (b5) 1200. The band width of the Gaussian kernel estimate is $h = 1$ ms. Vertical gray lines pass minima of $R_w(t)$, and the minima of $R_s^{(I)}(t)$ [$R_w(t)$] are represented by solid (open) circles. Temporal cross-correlation functions $C_{I,J}(\tau)$ between the instantaneous sub-population spike rate kernel estimates $R_s^{(I)}(t)$ and $R_s^{(J)}(t)$ of the sub-networks I and J : modular sparse synchronization for $J_{inter} =$ (c1) 10, (c2) 30, and (c3) 70, and global sparse synchronization for $J_{inter} =$ (c4) 400 and (c5) 1500. (d) Plot of the cross-correlation modularity measure $\langle C_M \rangle_r$ versus J_{inter} . The cross-correlation modularity measure $\langle C_M \rangle_r$ is obtained through average over 20 realizations, and the number of data used for the calculation of each temporal cross-correlation function $C_{I,J}(\tau)$ in each realization is 4×10^3 .

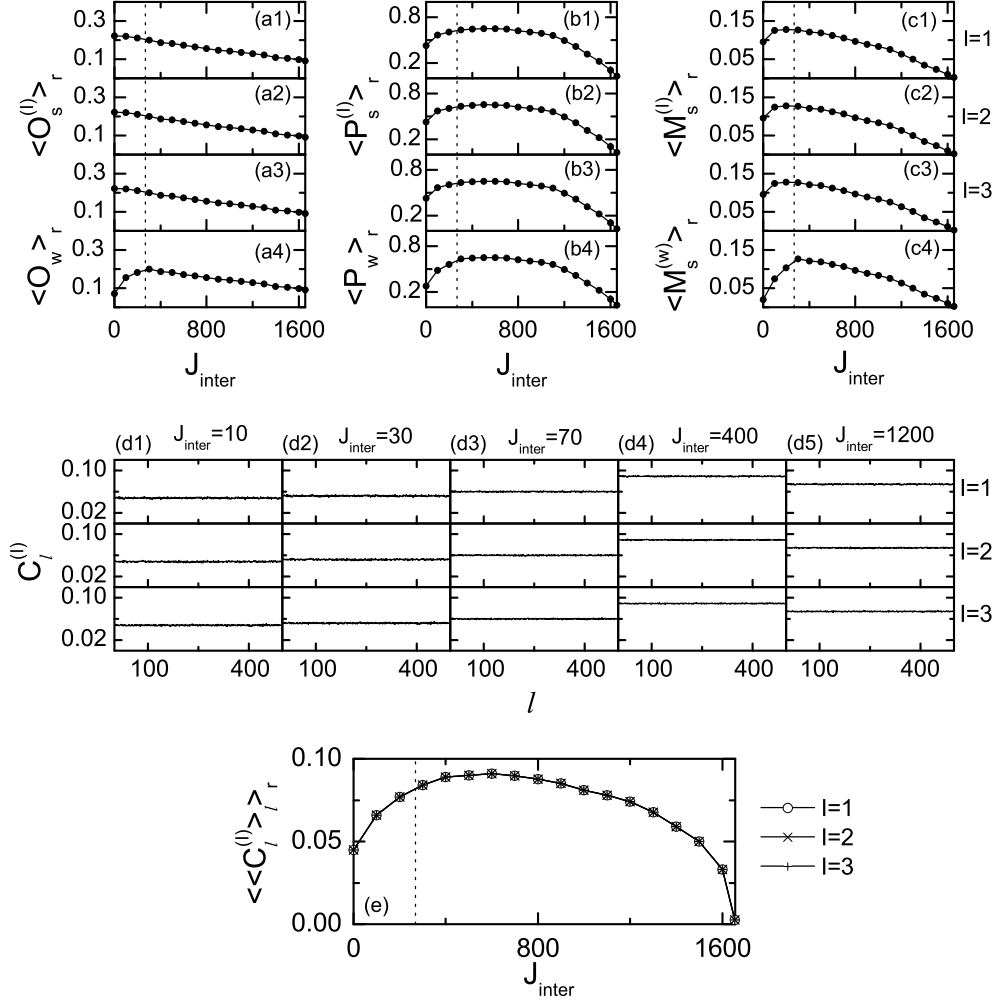


FIG. 7: Realistic statistical-mechanical spiking measure for measurement of the degree of modular and global sparse synchronization in the clustered network with 3 small-world sub-networks, each of them containing $L(=10^3)$ FS Izhikevich interneurons for $M_{syn}^{(inter)} = 20$ [route I in Fig. 3(g)] in the case of $I_{DC} = 1500$, $D = 500$, $M_{syn}^{(intra)} = 50$, $p_{rewiring} = 0.25$, and $J_{intra} = 1400$. Vertical dotted lines in (a1)-(c4) and (e) represent the threshold of $J = J_{inter}^* (\simeq 268)$. (a1)-(a4) Plots of the sub- and the whole-population occupation degrees $\langle O_s^{(I)} \rangle_r$ and $\langle O_w \rangle_r$ versus J_{inter} . (b1)-(b4) Plots of the sub- and the whole-population pacing degrees $\langle P_s^{(I)} \rangle_r$ and $\langle P_w \rangle_r$ versus J_{inter} . (c1)-(c4) Plots of the sub- and the whole-population statistical-mechanical spiking measures $\langle M_s^{(I)} \rangle_r$ and $\langle M_s^{(w)} \rangle_r$ versus J_{inter} . For each J_{inter} , we follow 3×10^3 global cycles in each realization, and obtain average occupation degrees, average pacing degrees, and average statistical-mechanical spiking measures via average over 20 realizations. Spatial cross-correlation functions $C_l^{(I)}$ in the three sub-networks: modular sparse synchronization for $J_{inter} =$ (d1) 10, (d2) 30, and (d3) 70 and global sparse synchronization for $J_{inter} =$ (d4) 400 and (d5) 1200. (e) Plot of the spatial cross-correlation degree $\langle \langle C_l^{(I)} \rangle_l \rangle_r$ versus J_{inter} . The spatial correlation degree $\langle \langle C_l^{(I)} \rangle_l \rangle_r$ is obtained through average over 20 realizations, and the number of data used for the calculation of each temporal cross-correlation function $C_{i,j}^{(I)}(\tau)$ in each realization is 4×10^3 .

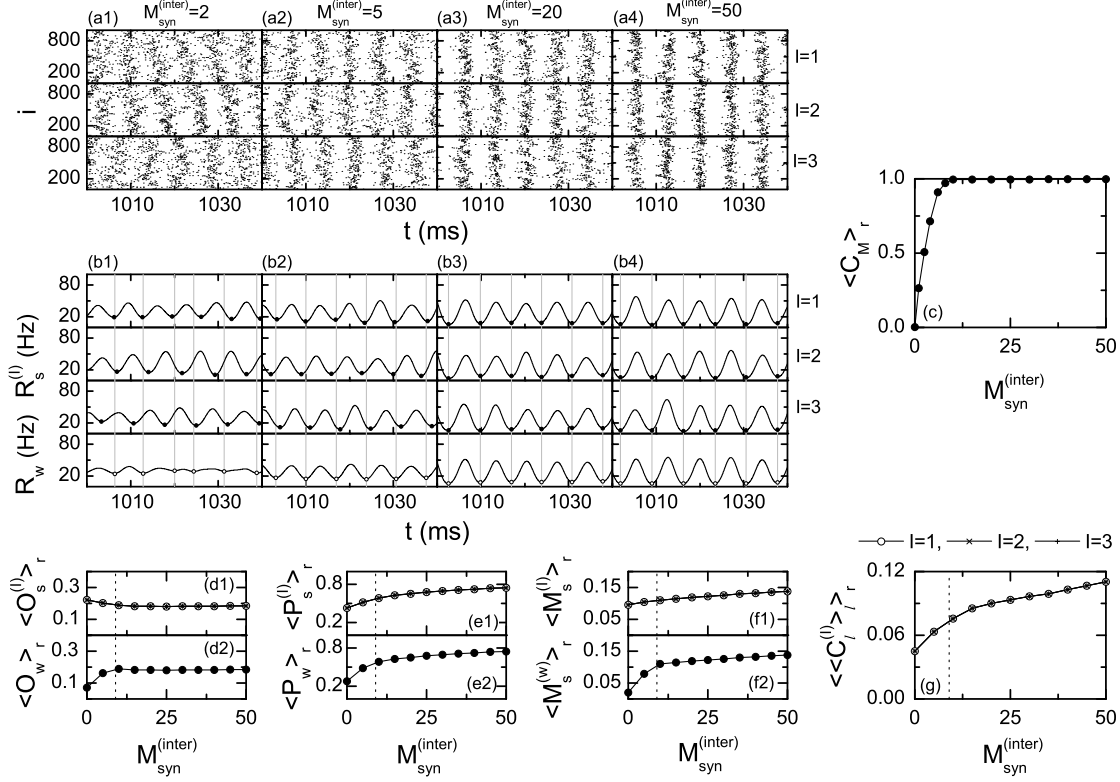


FIG. 8: Modular and global sparse synchronization in the clustered network with 3 small-world sub-networks, each of them containing $L (= 10^3)$ FS Izhikevich interneurons for $J_{inter} = 500$ [route II in Fig. 3(g)] in the case of $I_{DC} = 1500$, $D = 500$, $M_{syn}^{(intra)} = 50$, $p_{rewiring} = 0.25$, and $J_{intra} = 1400$. Raster plots of neural spikes in the sub-networks ($I = 1, 2, 3$): modular sparse synchronization for $M_{syn}^{(inter)} = (a1) 2$ and $(a2) 5$ and global sparse synchronization for $M_{syn}^{(inter)} = (a3) 20$ and $(a4) 50$. Instantaneous sub- and whole-population spike rate kernel estimates $R_s^{(I)}(t)$ ($I = 1, 2, 3$) and $R_w(t)$: modular sparse synchronization for $M_{syn}^{(inter)} = (b1) 2$ and $(b2) 5$ and global sparse synchronization for $M_{syn}^{(inter)} = (b3) 20$ and $(b4) 50$. The band width of the Gaussian kernel estimate is $h = 1$ ms. Vertical gray lines pass minima of $R_w(t)$, and the minima of $R_s^{(I)}(t)$ [$R_w(t)$] are represented by solid (open) circles. (c) Plot of the cross-correlation modularity measure $\langle C_M \rangle_r$ versus $M_{syn}^{(inter)}$. The cross-correlation modularity measure $\langle C_M \rangle_r$ is obtained through average over 20 realizations, and the number of data used for the calculation of each temporal cross-correlation function $C_{I,J}(\tau)$ in each realization is 2×10^4 . Vertical dotted lines in (d1)-(g) denote the threshold $M_{syn}^{(inter)*} (\simeq 9)$. (d1)-(d2) Plots of the sub- and whole-population occupation degrees $\langle O_s^{(I)} \rangle_r$ and $\langle O_w \rangle_r$ versus $M_{syn}^{(inter)}$. (e1)-(e2) Plots of the sub- and the whole-population pacing degrees $\langle P_s^{(I)} \rangle_r$ and $\langle P_w \rangle_r$ versus $M_{syn}^{(inter)}$. (f1)-(f2) Plots of the sub- and the whole-population statistical-mechanical spiking measures $\langle M_s^{(I)} \rangle_r$ and $\langle M_s^{(w)} \rangle_r$ versus $M_{syn}^{(inter)}$. For each $M_{syn}^{(inter)}$, we follow 3×10^3 global cycles in each realization, and obtain average occupation degrees, average pacing degrees, and average statistical-mechanical spiking measures via average over 20 realizations. (g) Plot of the spatial cross-correlation degree $\langle \langle C_l^{(I)} \rangle_l \rangle_r$ versus $M_{syn}^{(inter)}$. The spatial cross-correlation degree $\langle \langle C_l^{(I)} \rangle_l \rangle_r$ is obtained through average over 20 realizations, and the number of data used for the calculation of each temporal cross-correlation function $C_{i,j}^{(I)}(\tau)$ in each realization is 4×10^3 .

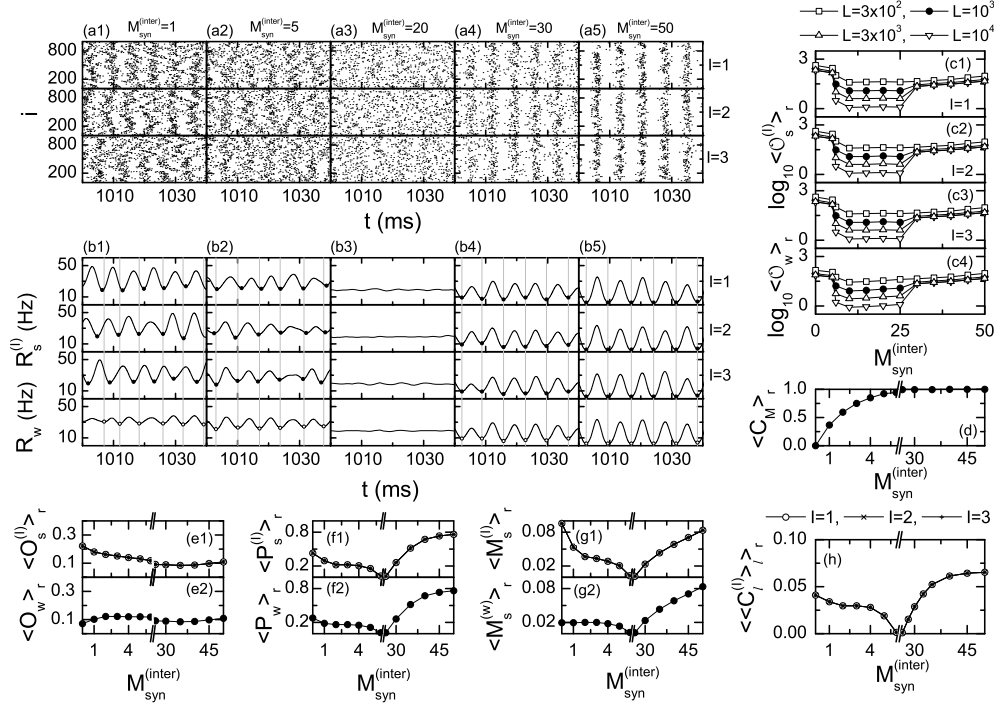


FIG. 9: Modular and global sparse synchronization in the clustered network with 3 small-world sub-networks, each of them containing L FS Izhikevich interneurons for $J_{inter} = 2500$ [route III in Fig. 3(g)] in the case of $I_{DC} = 1500$, $D = 500$, $M_{syn}^{(intra)} = 50$, $p_{rewiring} = 0.25$, and $J_{intra} = 1400$. Raster plots of neural spikes in the sub-networks ($I = 1, 2, 3$): modular sparse synchronization for $M_{syn}^{(inter)} =$ (a1) 1 and (a2) 5, unsynchronization for (a3) $M_{syn}^{(inter)} = 20$, and global sparse synchronization for $M_{syn}^{(inter)} =$ (a4) 30 and (a5) 50. Instantaneous sub- and whole-population spike rate kernel estimates $R_s^{(I)}(t)$ ($I = 1, 2, 3$) and $R_w(t)$: modular sparse synchronization for $M_{syn}^{(inter)} =$ (b1) 1 and (b2) 5, unsynchronization for (b3) $M_{syn}^{(inter)} = 20$, and global sparse synchronization for $M_{syn}^{(inter)} =$ (b4) 30 and (b5) 50. The band width of the Gaussian kernel estimate is $h = 1$ ms. Vertical gray lines pass minima of $R_w(t)$, and the minima of $R_s^{(I)}(t)$ [$R_w(t)$] are represented by solid (open) circles. (c1)-(c4) Plots of the sub- and the whole-population order parameters $\log_{10} \langle O_s^{(I)} \rangle_r$ ($I = 1, 2, 3$) and $\log_{10} \langle O_w \rangle_r$ versus $M_{syn}^{(inter)}$. For each $M_{syn}^{(inter)}$, the order parameter is obtained through average over 20 realizations, and the averaging time for the calculation of the order parameter in each realization is 4×10^3 ms. In (d)-(h), break symbols are given in the unsynchronization regions; the left (right) parts of the break symbols correspond to the regions of modular (global) synchronization. (d) Plot of the cross-correlation modularity measure $\langle C_M \rangle_r$ versus $M_{syn}^{(inter)}$. The cross-correlation modularity measure $\langle C_M \rangle_r$ is obtained through average over 20 realizations, and the number of data used for the calculation of each temporal cross-correlation function $C_{I,j}(\tau)$ in each realization is 4×10^3 . (e1)-(e2) Plots of the sub- and the whole-population occupation degrees $\langle O_s^{(I)} \rangle_r$ and $\langle O_w \rangle_r$ versus $M_{syn}^{(inter)}$. (f1)-(f2) Plots of the sub- and the whole-population pacing degrees $\langle P_s^{(I)} \rangle_r$ and $\langle P_w \rangle_r$ versus $M_{syn}^{(inter)}$. (g1)-(g2) Plots of the sub- and the whole-population statistical-mechanical spiking measures $\langle M_s^{(I)} \rangle_r$ and $\langle M_s^{(w)} \rangle_r$ versus $M_{syn}^{(inter)}$. For each $M_{syn}^{(inter)}$, we follow 3×10^3 global cycles in each realization, and obtain average occupation degrees, average pacing degrees, and average statistical-mechanical spiking measures via average over 20 realizations. (h) Plot of the spatial cross-correlation degree $\langle \langle C_l^{(I)} \rangle_l \rangle_r$ versus $M_{syn}^{(inter)}$. The spatial cross-correlation degree $\langle \langle C_l^{(I)} \rangle_l \rangle_r$ is obtained through average over 20 realizations, and the number of data used for the calculation of each temporal cross-correlation function $C_{i,j}^{(I)}(\tau)$ in each realization is 4×10^3 .

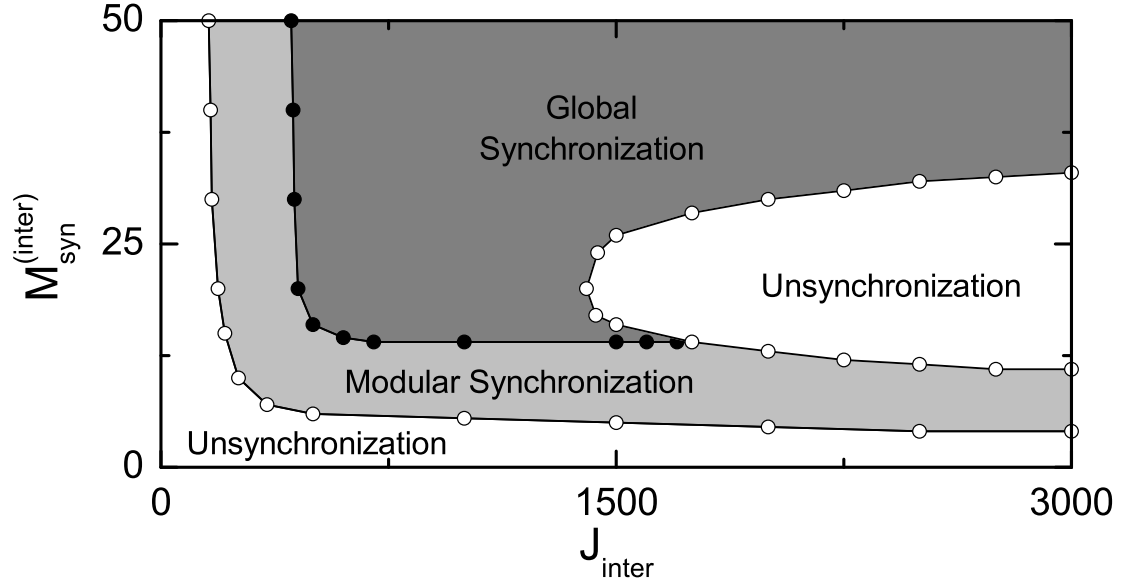


FIG. 10: State diagram in the $J_{\text{inter}} - M_{\text{syn}}^{(\text{inter})}$ plane for the 2nd case of the intra-modular dynamics (i.e., in the absence of inter-modular coupling, identically unsynchronized sub-networks with $p_{\text{rewiring}} = 0.05$) in the clustered network with 3 small-world sub-networks, each of them containing FS Izhikevich interneurons for $I_{DC} = 1500$, $D = 500$, $M_{\text{syn}}^{(\text{intra})} = 50$, and $J_{\text{intra}} = 1400$.

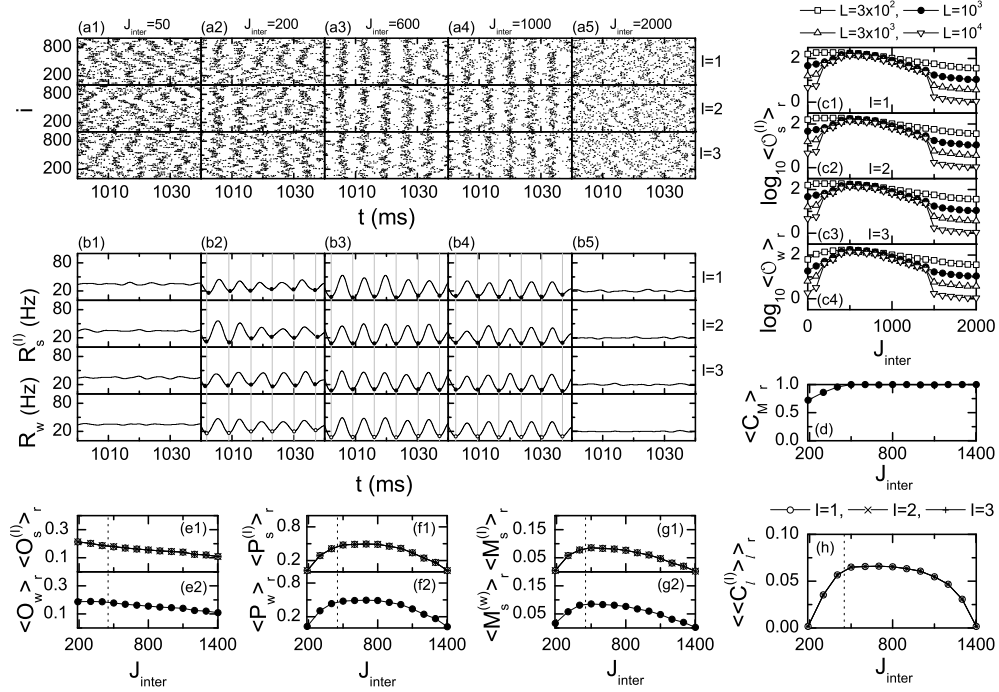


FIG. 11: Modular and global sparse synchronization for the 2nd case of the intra-modular dynamics (i.e., in the absence of inter-modular coupling, identically unsynchronized sub-networks with $p_{rewiring} = 0.05$) in the clustered network with 3 small-world sub-networks, each of them containing L FS Izhikevich interneurons for $M_{syn}^{(inter)} = 20$ in the case of $I_{DC} = 1500$, $D = 500$, $M_{syn}^{(intra)} = 50$, and $J_{intra} = 1400$. Raster plots of neural spikes in the sub-networks ($I = 1, 2, 3$): (a1) unsynchronization for $J_{inter} = 50$, (a2) modular sparse synchronization for $J_{inter} = 200$, global sparse synchronization for $J_{inter} =$ (a3) 600 and (a4) 1000, and (a5) unsynchronization for $J_{inter} = 2000$. Instantaneous sub- and whole-population spike rate kernel estimates $R_s^{(I)}(t)$ ($I = 1, 2, 3$) and $R_w(t)$: (b1) unsynchronization for $J_{inter} = 50$, (b2) modular sparse synchronization for $J_{inter} = 200$, global sparse synchronization for $J_{inter} =$ (b3) 600 and (b4) 1000, and (b5) unsynchronization for $J_{inter} = 2000$. The band width of the Gaussian kernel estimate is $h = 1$ ms. Vertical gray lines pass minima of $R_w(t)$, and the minima of $R_s^{(I)}(t)$ [$R_w(t)$] are represented by solid (open) circles. (c1)-(c4) Plots of the sub- and the whole-population order parameters $\log_{10} \langle \mathcal{O}_s^{(I)} \rangle_r$ ($I = 1, 2, 3$) and $\log_{10} \langle \mathcal{O}_w \rangle_r$ versus J_{inter} . For each J_{inter} , the order parameter is obtained through average over 20 realizations, and the averaging time for the calculation of the order parameter in each realization is 4×10^3 ms. (d) Plot of the cross-correlation modularity measure $\langle C_M \rangle_r$ versus J_{inter} . The cross-correlation modularity measure $\langle C_M \rangle_r$ is obtained through average over 20 realizations, and the number of data used for the calculation of each temporal cross-correlation function $C_{I,J}(\tau)$ in each realization is 4×10^3 . Vertical dotted lines in (e1)-(h) represent the threshold of $J = J_{inter}^* (\simeq 451)$. (e1)-(e2) Plots of the sub- and the whole-population occupation degrees $\langle \mathcal{O}_s^{(I)} \rangle_r$ and $\langle \mathcal{O}_w \rangle_r$ versus J_{inter} . (f1)-(f2) Plots of the sub- and the whole-population pacing degrees $\langle \mathcal{P}_s^{(I)} \rangle_r$ and $\langle \mathcal{P}_w \rangle_r$ versus J_{inter} . (g1)-(g2) Plots of the sub- and the whole-population statistical-mechanical spiking measures $\langle M_s^{(I)} \rangle_r$ and $\langle M_s^{(w)} \rangle_r$ versus J_{inter} . For each J_{inter} , we follow 3×10^3 global cycles in each realization, and obtain average occupation degrees, average pacing degrees, and average statistical-mechanical spiking measures via average over 20 realizations. (h) Plot of the spatial cross-correlation degree $\langle \langle C_l^{(I)} \rangle_l \rangle_r$ versus J_{inter} . The spatial cross-correlation degree $\langle \langle C_l^{(I)} \rangle_l \rangle_r$ is obtained through average over 20 realizations, and the number of data used for the calculation of each temporal cross-correlation function $C_{i,j}^{(I)}(\tau)$ in each realization is 4×10^3 .

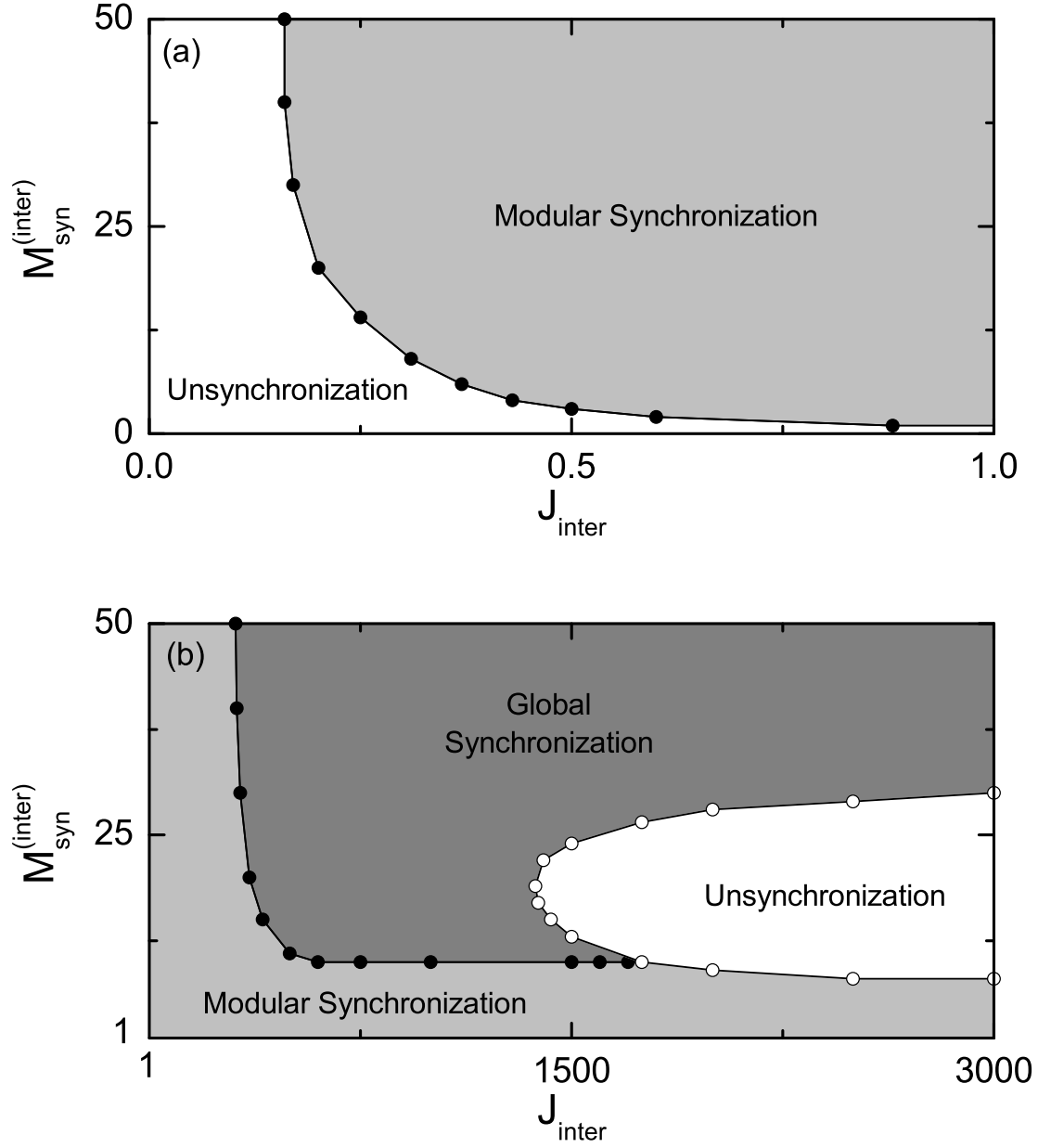


FIG. 12: 3rd case of the intra-modular dynamics (i.e., non-identical sub-networks where $p_{rewiring} = 0.25, 0.15$, and 0.05 for $I = 1, 2$, and 3 , respectively) in the clustered network with 3 small-world sub-networks, each of them containing FS Izhikevich interneurons for $I_{DC} = 1500$, $D = 500$, $M_{syn}^{(intra)} = 50$, and $J_{intra} = 1400$. (a) State diagram for the 3rd sub-network. For each $M_{syn}^{(inter)} \geq 1$, a transition to synchronization occurs in the 3rd sub-network when passing the threshold J_{inter}^{th} , denoted by solid circles. (b) State diagram in the J_{inter} - $M_{syn}^{(inter)}$ plane for the whole system.

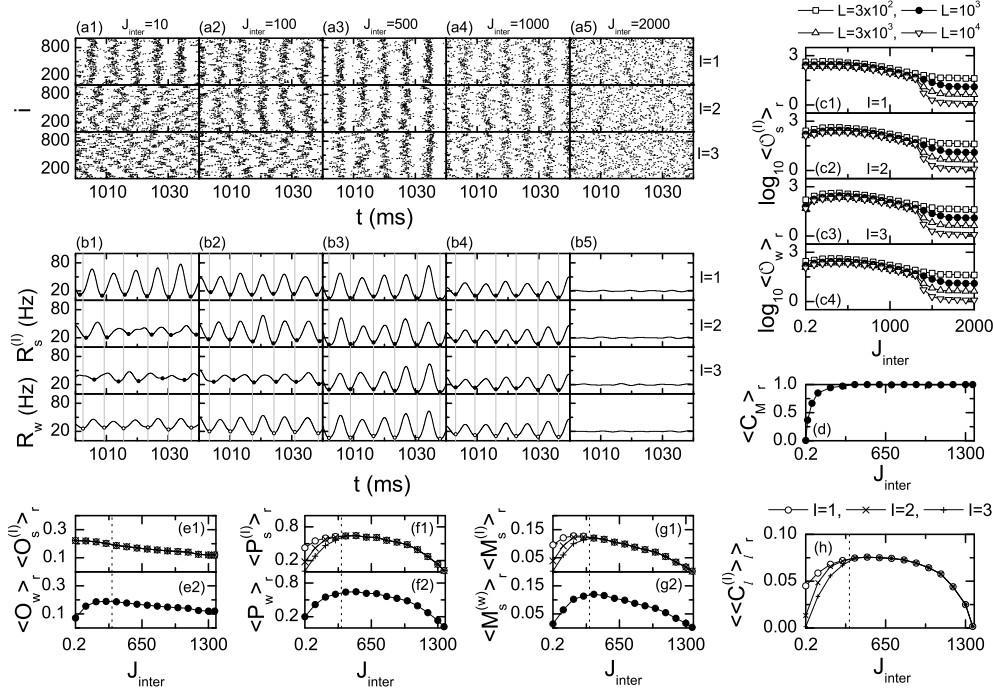


FIG. 13: Modular and global sparse synchronization for the 3rd case of the intra-modular dynamics (i.e., non-identical sub-networks where $p_{rewiring} = 0.25, 0.15$, and 0.05 for $I = 1, 2$, and 3 , respectively) in the clustered network with 3 small-world sub-networks, each of them containing L FS Izhikevich interneurons for $M_{syn}^{(inter)} = 20$ in the case of $I_{DC} = 1500$, $D = 500$, $M_{syn}^{(intra)} = 50$, and $J_{intra} = 1400$. For the case of $M_{syn}^{(inter)} = 20$, the 3rd sub-network becomes synchronized when passing the threshold $J_{inter,l}^* \simeq 0.2$. Raster plots of neural spikes in the sub-networks ($I = 1, 2, 3$): modular sparse synchronization for $J_{inter} =$ (a1) 10 and (a2) 100, global sparse synchronization for $J_{inter} =$ (a3) 500 and (a4) 1000, and (a5) unsynchronization for $J_{inter} = 2000$. Instantaneous sub- and whole-population spike rate kernel estimates $R_s^{(I)}(t)$ ($I = 1, 2, 3$) and $R_w(t)$: modular sparse synchronization for $J_{inter} =$ (b1) 10 and (b2) 100, global sparse synchronization for $J_{inter} =$ (b3) 500 and (b4) 1000, and (b5) unsynchronization for $J_{inter} = 2000$. The band width of the Gaussian kernel estimate is $h = 1$ ms. Vertical gray lines pass minima of $R_w(t)$, and the minima of $R_s^{(I)}(t)$ [$R_w(t)$] are represented by solid (open) circles. (c1)-(c4) Plots of the sub- and the whole-population order parameters $\log_{10} \langle \mathcal{O}_s^{(I)} \rangle_r$ ($I = 1, 2, 3$) and $\log_{10} \langle \mathcal{O}_w \rangle_r$ versus J_{inter} . For each J_{inter} , the order parameter is obtained through average over 20 realizations, and the averaging time for the calculation of the order parameter in each realization is 4×10^3 ms. (d) Plot of the cross-correlation modularity measure $\langle C_M \rangle_r$ versus J_{inter} . The cross-correlation modularity measure $\langle C_M \rangle_r$ is obtained through average over 20 realizations, and the number of data used for the calculation of each temporal cross-correlation function $C_{I,J}(\tau)$ in each realization is 4×10^3 . Vertical dotted lines in (e1)-(h) represent the threshold of $J = J_{inter}^* (\simeq 357)$. (e1)-(e2) Plots of the sub- and the whole-population occupation degrees $\langle \mathcal{O}_s^{(I)} \rangle_r$ and $\langle \mathcal{O}_w \rangle_r$ versus J_{inter} . (f1)-(f2) Plots of the sub- and the whole-population pacing degrees $\langle P_s^{(I)} \rangle_r$ and $\langle P_w \rangle_r$ versus J_{inter} . (g1)-(g2) Plots of the sub- and the whole-population statistical-mechanical spiking measures $\langle M_s^{(I)} \rangle_r$ and $\langle M_s^{(w)} \rangle_r$ versus J_{inter} . For each J_{inter} , we follow 3×10^3 global cycles in each realization, and obtain average occupation degrees, average pacing degrees, and average statistical-mechanical spiking measures via average over 20 realizations. (h) Plot of the spatial cross-correlation degree $\langle \langle C_l^{(I)} \rangle_l \rangle_r$ versus J_{inter} . The spatial cross-correlation degree $\langle \langle C_l^{(I)} \rangle_l \rangle_r$ is obtained through average over 20 realizations, and the number of data used for the calculation of each temporal cross-correlation function $C_{i,j}^{(I)}(\tau)$ in each realization is 4×10^3 .